Performance of the ATLAS Hadronic Endcap Calorimeter Modules to Electrons and Pions from 1999 Beam Test Data

Dominique Fortin[1], Michel Lefebvre[2]

University of Victoria,
Victoria, Canada.

May 4, 2001

Abstract

During the summer of 1999, the first six production modules of the Hadronic End-cap Calorimeter were assembled and installed in a beam test cryostat at CERN. In this note, the performance of the calorimeter is assessed in terms of its response and resolution to electrons and pions. The calorimeter is evaluated at five impact points and over an energy range of 10 to 200 GeV. The linearity of the response to electrons is observed to be within approximately one percent, and the average electromagnetic scale constant is measured to be $\alpha_{em} = (3.82 \pm 0.04)$ GeV/nA. The intrinsic (i.e. electronic noise subtracted) energy resolution obtained is $\frac{\sigma}{E} = \frac{(23.29\pm0.09)\%}{\sqrt{E_0(\text{GeV})}} \oplus (0.00 \pm 0.13)\%$ for electrons, and $\frac{\sigma}{E} = \frac{(76.2\pm09)\%}{\sqrt{E_0(\text{GeV})}} \oplus (6.68 \pm 0.09)\%$ for pions, where E_0 is the incident particle energy. Comparison with Monte Carlo simulations and the effect of the electronics calibration procedure are discussed. Finally, the ratio of electromagnetic to hadronic response, e/h, is measured to be $e/h = (1.509 \pm 0.021)$.

[1] fortin@pp.phys.uvic.ca
[2] lefebvre@uvic.ca

1   Introduction

The ATLAS Hadronic Endcap Calorimeter (HEC) is a liquid argon sampling calorimeter with copper plates as absorbers [1]. During the summer of 1999, 6 complete modules (3 front and 3 rear wheel modules), or 3/32 of one endcap, were assembled and set in a beam test cryostat. This was the first time that production modules (modules which will be used in the construction of ATLAS) were tested and the first time that the ATLAS calibration procedure and cabling system were used. In April and August of 1998, the first Hadronic Endcap modules built to the final ATLAS design specifications were tested. But with only four ϕ segments, lateral leakage of hadronic showers occurred [2]. Negligible lateral leakage was expected in 1999 for beams centered on the calorimeter.

Beam tests are essential to control the quality of the production and in evaluating the performance of the calorimeter. In this work, the energy scans performed with electron and pion beams at several impact positions are studied to assess the energy response and resolution of the calorimeter. These results are compared with the values obtained by Monte Carlo simulations. Vertical and horizontal electron beam scans are also used to determine the spatial uniformity of the calorimeter response.

In Section 2, an overview of the HEC and of the experimental setup is made. Sections 3 and 4 summarizes the results obtained for the calorimeter response and resolution to electron and pion beams respectively. Finally, the electromagnetic to hadronic response ratio obtained in this analysis is also presented in Section 4.

2   Overview of the Experiment

2.1   Setup

The beam tests were conducted on the H6 beam line of the SPS at CERN. The modules of the Hadronic Endcap were installed in a cryostat which was later filled with liquid argon (LAr) maintained at (90.0 ± 0.1) K. Several subdetectors, such as trigger counters and multi-wire proportional chambers, were installed in the beam-

line to track particles. This section describes the beam test setup: the layout of the modules, the trigger system, the processes followed for readout and calibration, and finally, the various particle beams used.

2.1.1 Modules layout

During the 1999 beam tests, the calorimeter was segmented in 4 readout depths: two in the front wheel (z=1 and z=2) and two in the rear wheel (z=3 and z=4). The first readout segment (z=1) consists of 8 LAr gaps, each separated by 2.5 cm of copper. The second segment (z=2) consists of 16 LAr gaps also separated by 2.5 cm of copper. Both of the last two readout segments (z=3 and z=4) consist of 8 LAr gaps separated by 5 cm of copper. A readout cell is defined as a pointing tower spanning a longitudinal readout segment. Figure 1 shows the layout of the readout cells for the first depth. The cryostat window, the region where the beam could be set to enter the calorimeter, is also indicated. The beam was set to enter the calorimeter at different locations, or impact points. In this work, 5 impact points were studied and correspond to beams centered on readout cells 61, 57, 37, 33, and 29. These impacts are referred to as impact B, C, F, G and H, respectively.

The Hadronic Endcap calorimeter is designed to provide a semi-pointing geometry in pseudorapidity. However, because of space constraints within the cryostat, the modules could not be positioned in the proper pointing orientation. Instead, the beam entered parallel to the symmetry axis which resulted in showers depositing energy in a larger number of cells than they would in ATLAS (see Figure 2). As a consequence, the reconstruction of the energy required larger clusters (groups of cells), which means that the electronic noise contribution to the energy resolution is increased compared to what it would be for ATLAS.

2.1.2 Trigger system

In order to eliminate undesirable events, such as those caused by particles coming from the beam halo (periphery of the beam), several detectors were added in front and behind the cryostat. Figure 3 shows a schematic view of the setup giving the
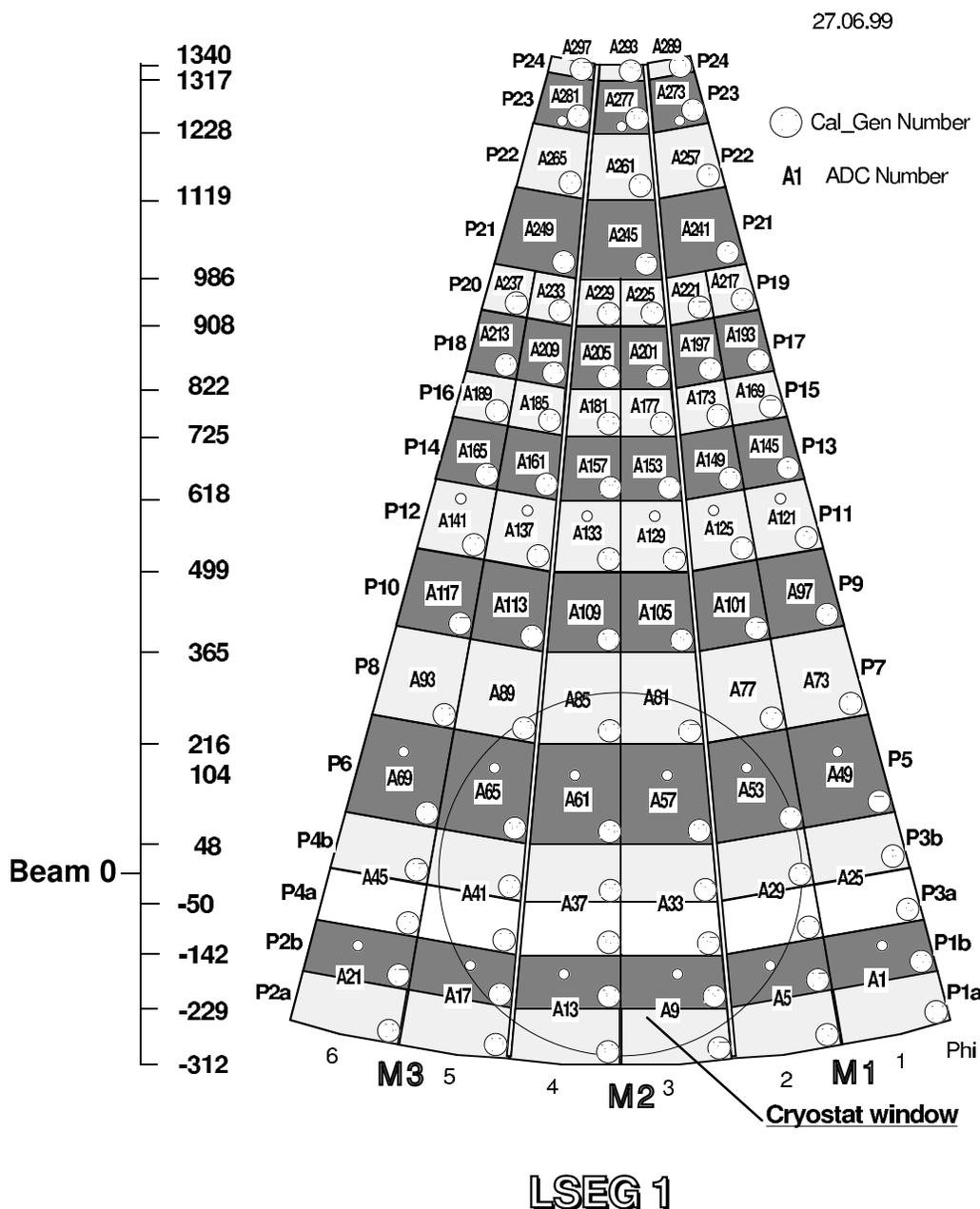
Figure 1: The geometric layout of the readout cells for the first depth (z=1) [3]. The beam enters in a direction perpendicular to the surface shown, in a region behind the cryostat window. The numbers appearing in the squares and preceded by an "A" are identifying the channels used for the readout cells; the circled numbers are identifying the channels from the calibration generator. The layout of the readout cells for the remaining 3 depths is presented in Appendix A. The impact points used in the analysis correspond to beams centered on readout cells 61, 57, 37, 33, 29 and are referred as impact points B, C, F, G and H, respectively. Scale in mm.
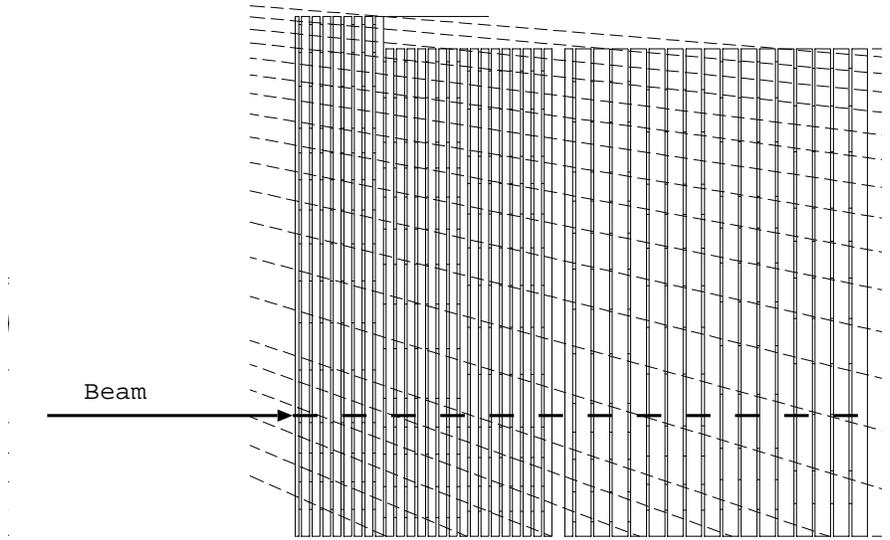
Figure 2: Comparison between the orientation of the beam and the semi-pointing geometry of the Hadronic Endcap calorimeter. The fine dashed lines represent possible trajectories of a particle traveling in a straight line from the ATLAS vertex (constant pseudorapidity). The readout cells are positioned accordingly to these pseudorapidity lines in a stepped fashion, creating a semi-pointing geometry. The thick line represents the incident particles during the 1999 beam tests.
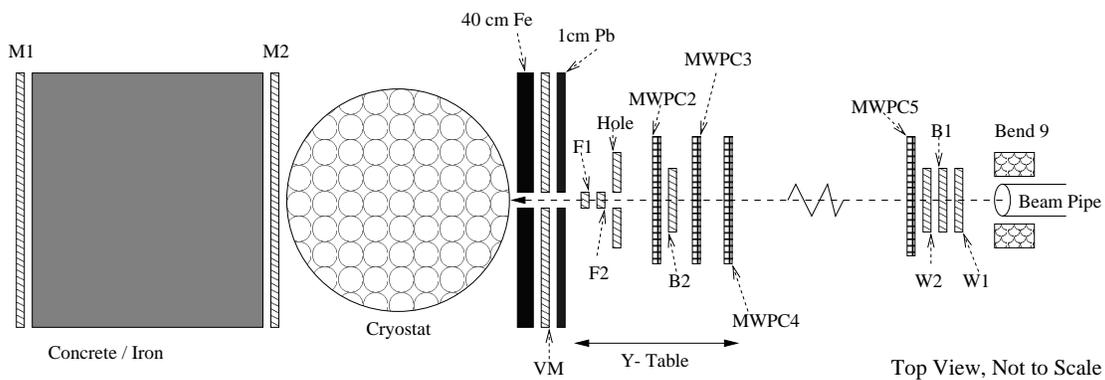

Figure 3: Setup of the HEC beam tests. The detectors shown in the diagram are: bend 9: final bending magnet; W1,B1,B2,W2: beam counters; MWPC : multi-wire proportional counters (beam chambers); F1,F2 and Hole: finger counters and Hole veto counter, which define the transverse size of the beam; VM: muon veto; M1,M2: muon counters.

location of the different triggering detectors. B1, F1 and F2 are scintillating detectors, located upstream from the cryostat. F1 and F2 are oriented perpendicularly to one another, and effectively define the transverse size of the beam (a square of about 2.5 cm × 2.5 cm). Both are mounted on a motorized table (y-table) which can be displaced in the vertical direction. VM and *hole* are both scintillating counters used to eliminate or "veto" particles from the beam "halo", that is, particles coming from the periphery of the beam creating a signal in the VM and hole counters.

The pre-trigger, or the presence of a signal in the B1, F1 and F2 detectors upstream from the cryostat, was the first condition to keep any event for this analysis. Also, events were not recorded whenever two events occurred too closely in time, creating an overlap of signal in the detector (pile-up). Finally, events arising from random triggers were discarded. Events passing all of the above cuts are called physics events.

Since the Cherenkov detector (CEDAR) efficiency is limited to low energy particles, it was impossible to distinguish electrons from pions via the trigger system for most of the runs. The CEDAR separates particles according to the Cherenkov opening angle and the difference between electron and pion angles gets smaller at higher energies. In practice the separation limit is around 80 GeV [4]. But, as it will be shown later, software selection criteria were sufficient.

M1 and *M2* are also scintillating detectors located behind the cryostat. They are used, together with the VM, to identify muons.

When studying the uniformity of the calorimeter (Section 3.6), the multi-wire proportional counters (beam chambers), each having a wire spacing of 1 mm, were also used to determine the exact location of the beam particle impact on the calorimeter. The position was calculated via the beam chamber reconstruction package included in the HEC beam test software package [5].
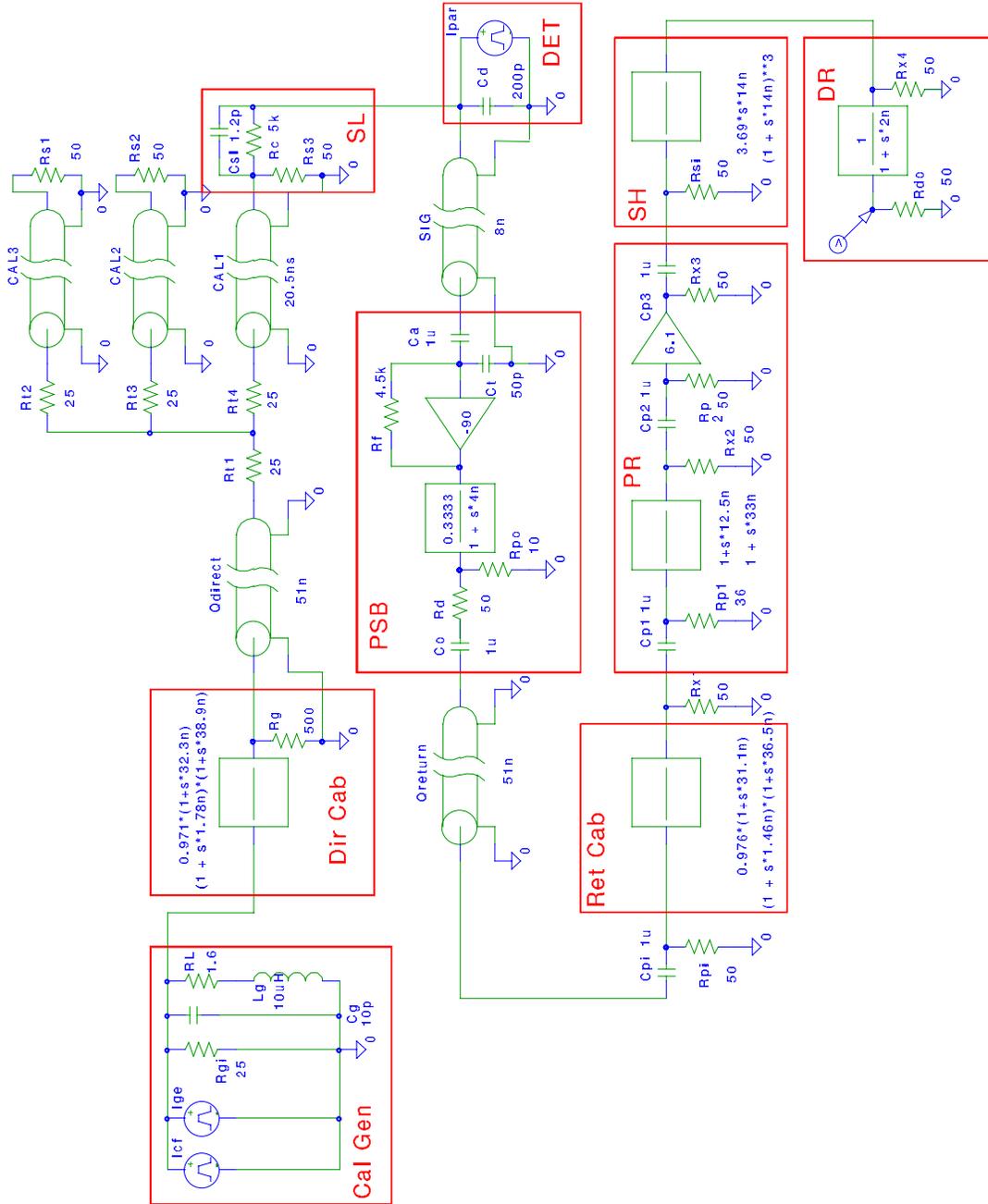
Figure 4: The various components of the HEC electronic chain as modeled for analytic calculation of its performance [7]. The calibration generators (Cal Gen) current is transmitted to the detector (DET) by the calibration cables (Dir Cab) and strip-lines (SL). The signals produced at the PAD boards (PSB) exit the cryostat via the return cables (Ret Cab) and are shaped by the FEB boards (preshaper (PR), shaper (SH), and driver (DR)). Finally, the signal is digitized by fast analog digital converter (flash ADC's) every 25 ns, and read out by the data acquisition system.

2.1.3 Readout and calibration

Figure 4 shows the various electronic components for the calibration and readout of the HEC during the 1999 beam test. The signal produced in each of the calorimeter readout cells is sent via what are known as return cables and the shapers of the Front End Boards (FEBs) before being read out by fast analog digital converters (flash ADC's). For the beam tests, the same cabling system as the one to be used in ATLAS (for example the same cable length) was installed. ATLAS FEBs, which contain the pre-shapers, shapers and line drivers, were used for the first time (see Figure 4). FEBs were installed for the beam tests shortly after they were produced, and hence were not fully studied until after the beam test period was over. Several problems were then noted: the gain and integration time of the pre-shapers were outside the design values, some of the shapers were not working properly, and finally, the drivers were observed to have a different transfer function than expected. These problems caused the readout of the channels close to the edge on the FEB connectors to have an increased level of noise. The signal reconstruction is discussed in detail in Section 2.2.

In order to obtain a relationship between the current measured on the readout boards and the electronic signal, each of the readout cells was calibrated individually. To do so, external calibration generators injected known current pulses to all of the readout electrode by a network of coaxial cables and strip lines. The relationship between the injected current and the resulting ADC's signal produced (after pedestal subraction and digital filtering, see Section 4.2) was then parameterized in terms of a 3rd order polynomial with different parameters for each readout cell. As a result, the cell-to-cell differences in the electronics gain were corrected. This calibration allows the energy in ADC counts to be converted to energy in units of current (nA) produced in the gaps by ionization [3].

In 1999, the ATLAS calibration procedure was followed for the first time [7]. Also, the length of the calibration cables were set to match exactly the length they

---

[3]Typically, 1 ADC count$\approx$50 nA and 1 nA$\approx$0.0038 GeV.

will be in ATLAS. To describe the calibration response of this new, more complicated chain, the old electronics model had to be improved substantially. Unfortunately, no modifications were made for the 1999 beam tests, which influenced the quality of the calibration. Recalibrating the HEC electronics was outside the scope of this work.

2.1.4 Beam production

450 GeV proton beams are produced in the SPS, the Super-Proton-Synchrotron. The H6 and H8 beam lines in the EHN1 experimental area (North Area) provide both secondary and tertiary electron, pion and muon beams by using a common target, and an array of magnets and collimators. The primary target is used to produce electrons and pions of a wide range of energies, the upper limits being 300 GeV for H8 and 200 GeV for H6 for standard running conditions.

Low momentum particle beams ($10 < p < 100$ GeV [4]) are produced when the H6 beam-line is used in tertiary mode, that is, when a second target is introduced into the beam-line. This second target is either a block of 9 mm thick lead (for pion selection), or a piece of polyethylene (for electron selection). In this mode, the first part of the beam (between the two targets) is tuned for the highest possible momentum (200 GeV), while the second part is tuned for the requested low momentum. Momenta from 10 to 80 GeV can be selected by the user simply by loading the corresponding beam files, which set the magnets and collimators properly. The drawback in using tertiary beams is a loss in intensity. Typical beam intensities range from a few 10^2 p.p.s (particle per second) for 10 GeV (tertiary) beams to a few 10^4 p.p.s for 200 GeV (secondary) beams [4].

The separation of electrons from hadrons ($\pi^\pm$) is achieved by synchrotron radiation energy loss in a series of magnets followed by the collimation of the hadrons. At 200 GeV, the separation is 16 mm at a distance of ~ 350 m [5]. The momentum

---

[4]The momentum throughout this note is always expressed in natural units: $\hbar = c = 1$.

[5]$\delta E = \frac{4\pi}{3}\frac{e^2}{R}\beta^3\gamma^4$ and $E = \gamma mc^2$ meaning that $\delta E \propto 1/m^4$. Therefore, synchrotron radiation loss is $\approx 10^{10}$ less in $\pi^\pm$ than in $e^\pm$.
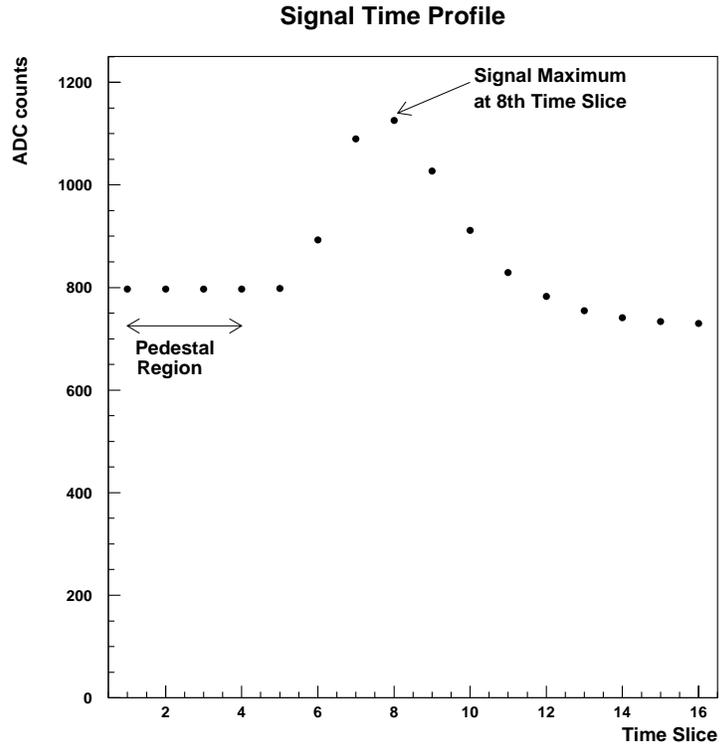
Signal Time Profile

Figure 5: Time profile of a typical readout cell signal from a sample (or slice) of the 1998 electron runs data [13]. The pedestal region (time samples 1-5) is important in calculating the electronic noise. In 1999, the timing of the signal maximum was set to occur in the 9th time sample to ensure that no signal was present in the pedestal region, and to study the electronic noise.

resolution is given by a set of two collimators and is of the order of $\delta p/p = 0.3\%$ for a standard setting of the collimators. This means that the error on the beam energy is negligible compared to the calorimeter resolution, and will thus be ignored in the analysis.

2.2   Signal reconstruction

As was mentioned in the previous section, the signal from each readout cell for each event is recorded in ADC counts every 25 ns for a total of 400 ns, or 16 time samples. In Figure 5, a typical signal shape from a data sample is shown. The first 5 time samples, called the pedestal region, occur before the signal rise and are used

Readout depth (z)	EM weights
1	1
2	1
3	2
4	2

Table 1: Electromagnetic (EM) depth weights applied to the readout cells for calibrated signals (nA). These weights originate from the difference in the sampling fraction between the front and rear wheels.

to compute the base level of the ADC for zero input, known as pedestals; the signal maximum was set to occur close to the 9th time sample.

From the readout cell signal time profile, the cell response is computed as follow:

- First, the pedestal is averaged over the entire run [6].

- The pedestal is then subtracted from the cell signal for all time samples.

- The digital filtering method (described in Section 2.2.2) is then applied to calculate the cell response.

- Finally, the response is converted from ADC counts to nA using the calibration coefficients.

Additional correction factors were also applied on the response of specific cells because of differences in sampling fraction and because of a few high voltage (HV) problems. The sampling fraction in the front wheel is twice that of the rear wheel so that, for showers, a factor of two must be applied to the energy measured in the third and fourth depths ($z=3$ and $z=4$). These depth weights are presented in Table 1.

Some HV problems were experienced during the 1999 beam test and required disconnecting five of the EST boards. The faulty EST boards were disconnected by turning off the corresponding HV channels from the HV generators. As it was shown

---

[6]Data was taken and recorded in runs, that is, files were created for each beam setup (same impact point, particle type and energy) and contained typically 10,000 events.

Module	Segment (z)	Correction factor
1	2	1.33
2	4	1.33
3	2	2.00
3	4	1.33

Table 2: Location of the disconnected EST boards, and corresponding correction factors. Note that in the second depth (z=2) of module 3, two EST boards were disconnected. Because of amplification problems, readout cell 61 needed an additional correction factor of 2.00.

in previous years, correction factors completely restore the response and resolution. The only noticeable consequence of the HV problems is a corresponding rise of electronic noise [2] [6]. In order to compute the correction factors, the number of HV channels turned off in each readout depth was taken into account. There are four HV sources per depth. Hence, if one (two) of the HV channels is turned off in a readout depth, 1/4 (1/2) of the signal is lost. The necessary correction factor is therefore 4/3 (4/2). HV correction factors are summarized in Table 2. The readout cell 61, located in the first depth of module 2, needed an additional correction factor of 2.00. This additional factor was necessary to correct for a damaged output connector [7].

A software package [5] was written to compute the response of the readout cells. In the following sections, the procedure used by this software package to calculate the pedestals and the energy deposited are discussed.

2.2.1 Pedestal computation

Different ways of evaluating the pedestals have been tested. In this work, the pedestals for each cell were determined from the average of the signal in the first time sample (in ADC counts) over all physics events (events that passed the triggers) within a run.

In previous analyses, the pedestals were calculated from random events (within particle runs) or from dedicated noise runs with no particle beam (see Section 2.3).

In both cases, the events were produced by software triggers when no beam was entering the calorimeter. The two methods led to different results, by an average of (0.3 ±0.1) ADC counts. Eventually, these two methods were discarded when it appeared that they were overestimating the pedestals, causing a large offset in the response. The pedestals used in this analysis (using the physics events) are compared with the pedestals obtained from random events in Figure 6. The pedestals from random events are shown to be overestimated on average by (2.5 ±0.1) ADC counts. This difference has not been understood.

2.2.2 Digital filtering

The digital filtering method applies weights, computed using the time sample autocorrelation function, to the signal of five time samples. It gives the best possible signal to noise ratio for the determination of the signal height and time for those 5 time samples [5] [8]. To calculate the response of the readout cell for a shower event, the digital filtering method is applied over the 5 time samples centered on the signal maximum (9th time sample).

2.3 Electronic noise

In order to verify the intrinsic characteristics of the Hadronic Endcap calorimeter, the electronic noise present in the response must be measured to extract the sampling and constant term from the overall energy resolution.

In this analysis, the electronic noise of a channel is evaluated from the distribution of the signal in the pedestal region over an entire run. The signal is obtained by applying the digital filtering method to the pedestal subracted ADC signal over the first 5 time samples for physics events, events which passed the trigger cuts (see Section 2.1.2). Also, the calibration coefficients, EM weights and correction factors used in calculating the cell response to showers were applied when needed (Section 2.2). The width of the distribution obtained was defined as the electronic noise. This process was then repeated with every particle beam run analyzed.
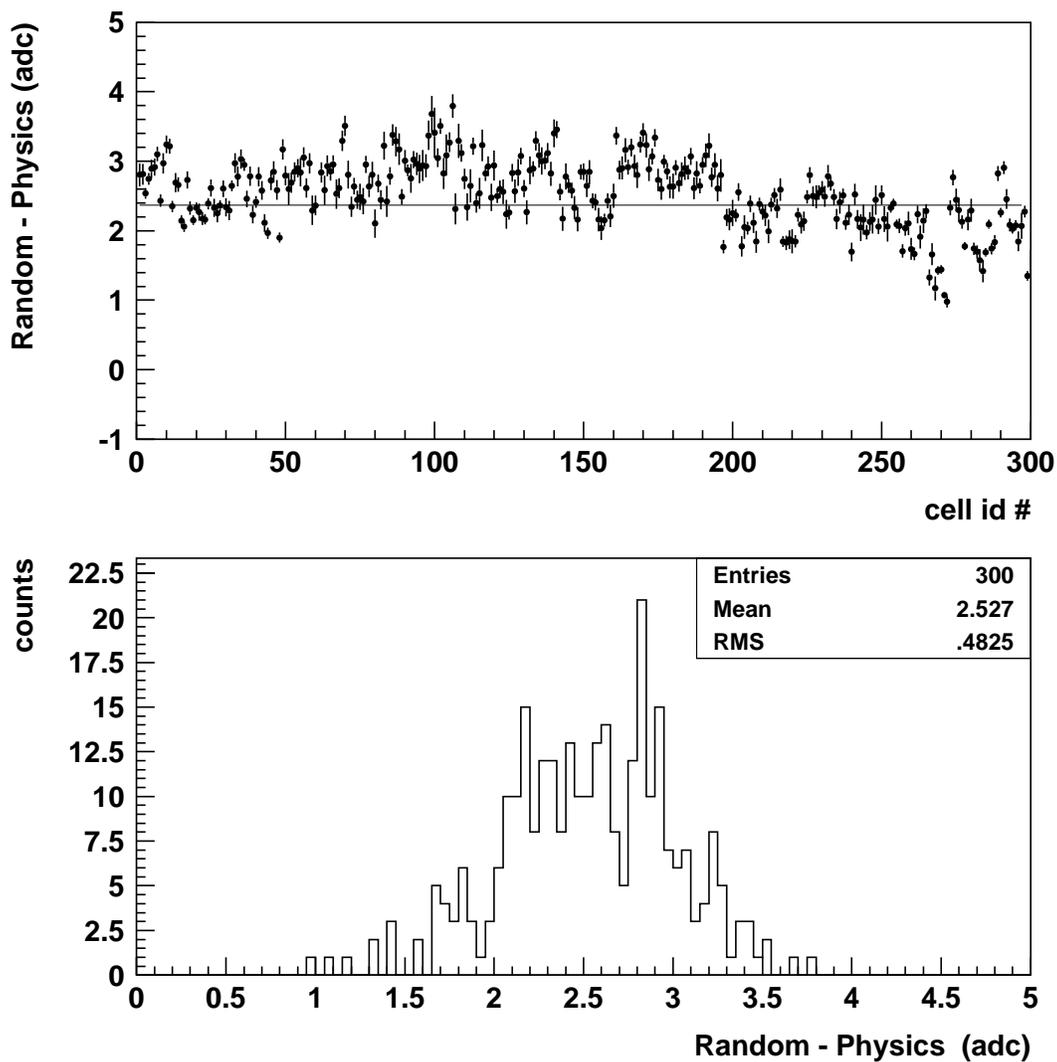
Figure 6: Difference in the value of the pedestals computed from random events and from physics events for run 9171 (193.1 GeV electrons at impact position C). The overall average difference is of (2.5 ±0.1) ADC counts. The error bars shown are purely statistical.

The distribution of the signal in the pedestal region (also referred to as noise distribution) was observed to be non-Gaussian. This is shown in Figure 7 for several cells, where non-Gaussian positive tails can be seen. It was also noted that the most probable value (current) of the distribution was non-zero and negative for most cells: between -20 and 0 nA (within errors). The variation in the noise values shown in Figure 7 can be explained by the channels in the second layer having twice as many gaps connected together than the other channels, resulting in a noise $\sqrt{2}$ times greater.

The energy deposited by an electromagnetic or hadronic shower as it propagates through the calorimeter is distributed over several cells that form a cluster. To reconstruct the energy of an electron or pion shower, the energy of each cell in the cluster must be summed. The cluster electronic noise will then have contributions from all the cluster cells. Figure 8 shows the cluster electronic noise for a 9 cell cluster used in the analysis of electron data. Here again, the electronic noise distribution displays a non-Gaussian positive tail and the most probable current is non-zero and negative. The cluster and cell noise distribution were found to be truly Gaussian on the negative side as shown in Figure 8. It was found that events with large cell noise lead to events with large cluster noise.

The cluster electronic noise in each event was then compared to the measured cluster energy as shown in Figure 9. An excess of events with high electronic noise can be observed on the high energy side of the cluster energy distribution. This excess shows the correlation between high electronic noise and high signal in the cluster.
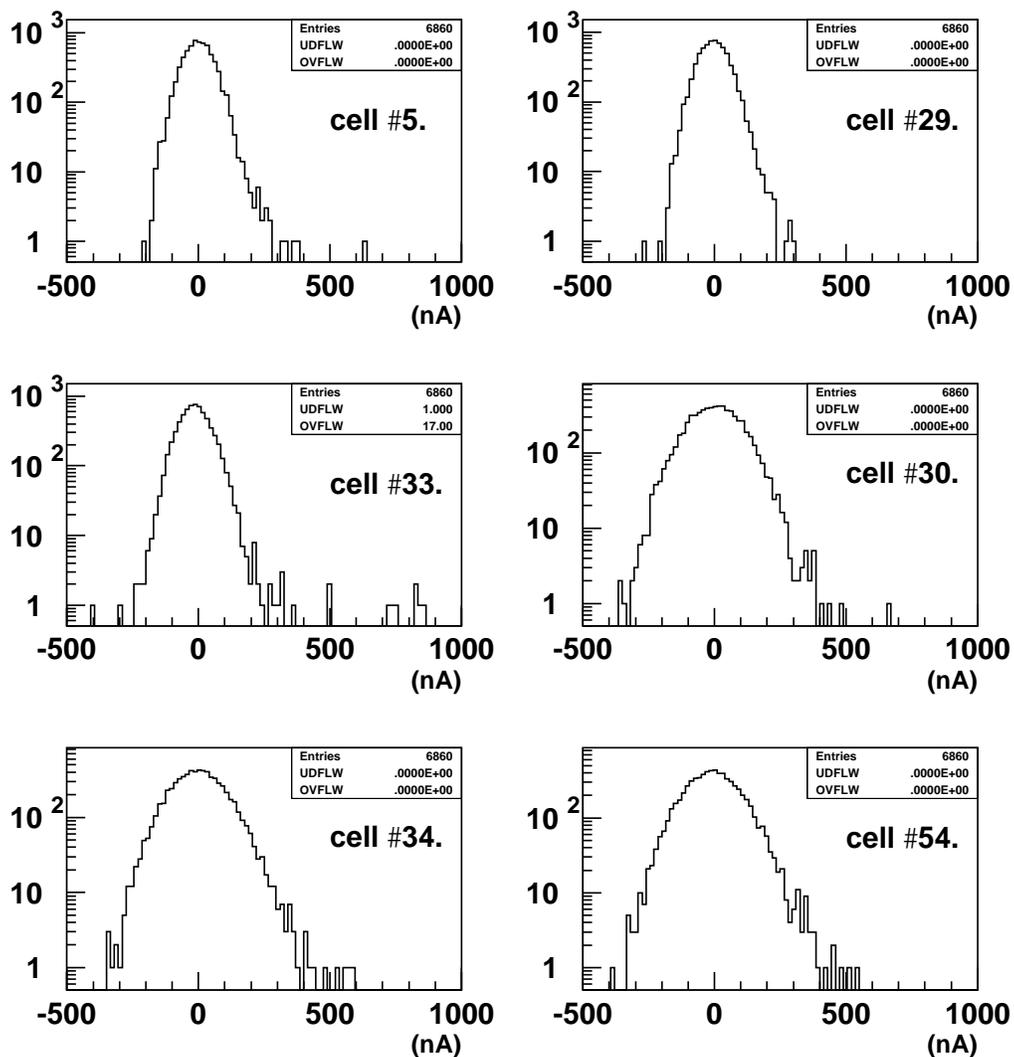
Figure 7: Distribution of the signal (in nA) in the pedestal region for various cells for run 9011 (10 GeV electrons). The width of these distribution is the electronic noise. For most cells, non-Gaussian positive tails are observed, and the most probable value of the distribution is negative. The cell identification number is also given. Note that cells 5, 29 and 33 are from the 1st depth; cells 30, 34 and 54 are from the 2nd depth (see Appendix A).
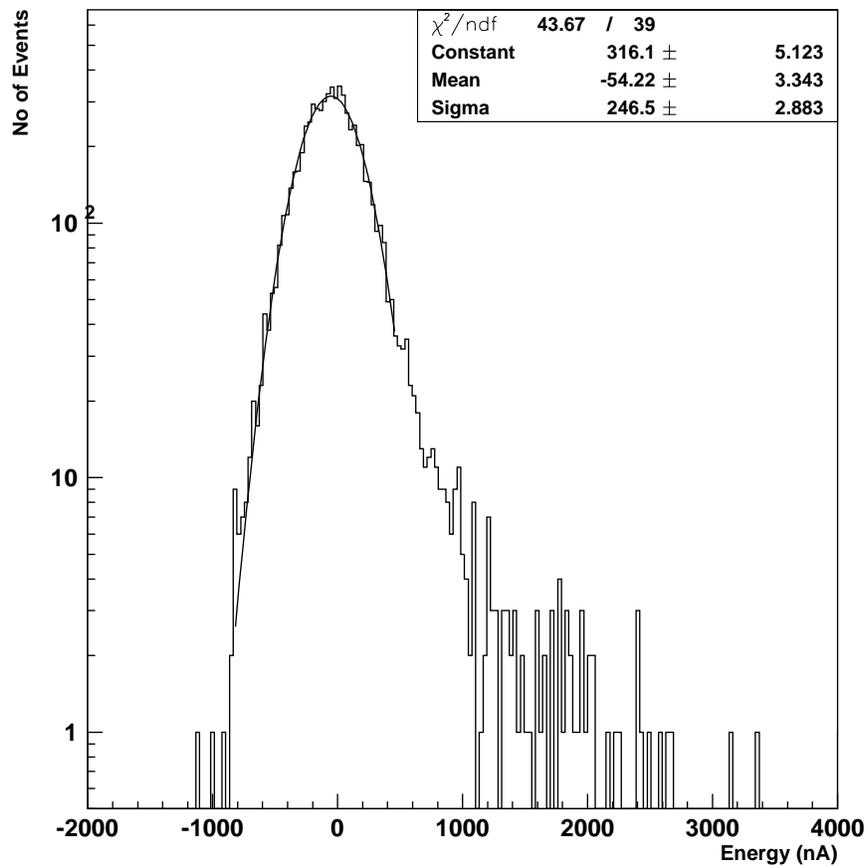
Figure 8: Cluster electronic noise in units of current for run 9011 (10 GeV electrons). The cluster is made of 9 readout cells. A non-Gaussian positive tail can be seen, and the most probable value of the distribution is negative. A Gaussian fit was performed on the region located between -3σ and $+2\sigma$ of the most probable current, and the distribution appears to be truly Gaussian on the negative side.
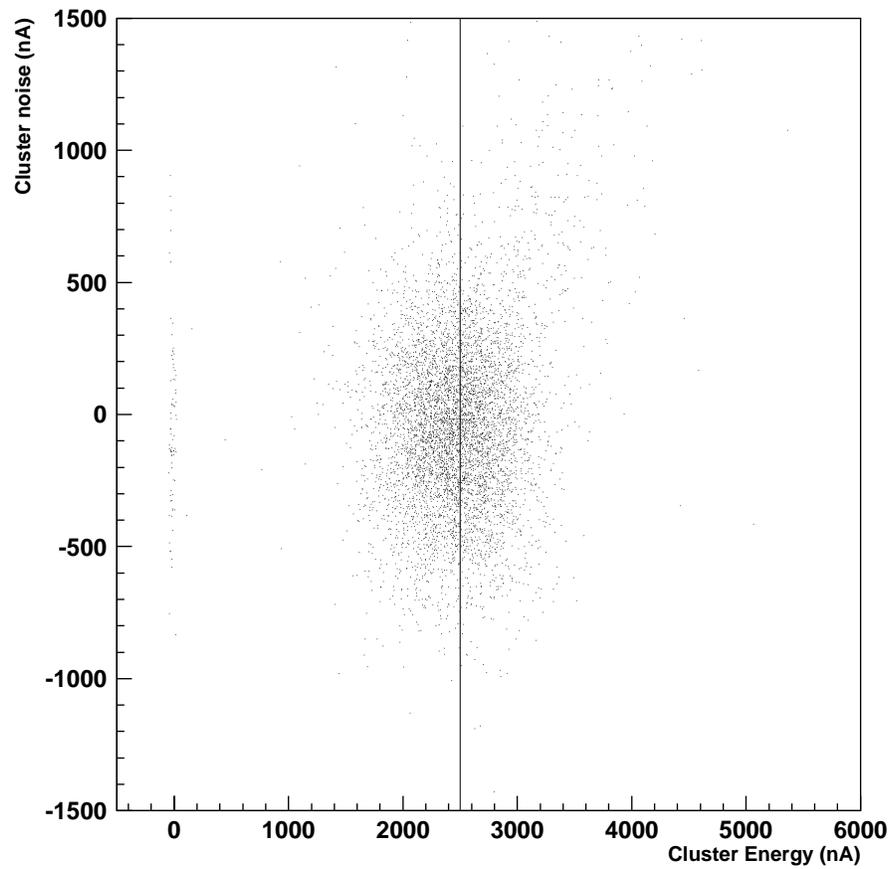
Figure 9: Cluster electronic noise vs. reconstructed energy in units of current for run 9011 (10 GeV electrons). The cluster is made of 9 readout cells. The vertical line shows the average energy in the cluster. A correlation between high electronic noise and high signal (energy) in the cluster can be observed.

The origin of the positive tails in the electronic noise distribution was investigated by asking the following questions :

- Are the tails caused by the digital filtering method ?

- Are the tails caused by the ADC to nA calibration ?

- Is there a leakage of the shower signal in the pedestal region of the signal time profile ?

Data analysis revealed that:

- The same distribution is present when the average signal over the first 5 times samples is used to calculate the noise, instead of using the digital filtering method.

- The same distribution is obtained by performing the analysis in ADC (that is without the use of calibrations), with or without applying the digital filtering method.

- The same distribution is present after removing the events for which the signal in the 5th time sample is the greatest of the 5.

Therefore, the hypotheses above failed to explain the problems observed in the electronic noise distribution. It is postulated that the positive non-Gaussian tails are caused by some positive signal [7] picked-up by all time samples for many events. This working hypothesis can explain the correlations between high electronic noise and high signal in the cluster.

To circumvent this problem in assessing the HEC intrinsic performance, Gaussian fits, for which the data range is not centered on the most probable value, are used to estimate the most probable current (μ) and the electronic noise (σ) of the true distribution. The asymmetric fits are first performed on a 4σ range at different locations over the distribution until a minimum χ^2 is reached. The systematic

---

[7]Overlap of events (pile-up) caused by undetected particles.

errors on μ and σ are estimated as the difference between this best asymmetric fit obtained and the values obtained from a Gaussian fit performed in the region $\pm 2\sigma$ about the most probable current. The values of μ and σ are presented in Figures 10 and 11 for all of the electron and pion runs, respectively. The clusters for electron and pion data analysis are described in Sections 3.2 and 4.2.

As can be seen in Figures 10 and 11, the electronic noise was not constant during the data taking period and is therefore found to depend on the beam energy. The exact causes of these noise variations are still unknown. It was first thought that temperature fluctuations in the experimental hall (especially the difference between day and night) might have affected the results, but no correlations were found between the temperature of the electronics and the noise. Similarly, no major changes in the liquid argon temperature nor in the EST boards voltage were observed. Further studies were made by electronic experts, and it was noted that the noise depended mainly on a few very noisy channels [7]. In these channels, instability in the pre-shapers, shapers, or line drivers of the FEBs caused the output signal to be either delayed and/or under-amplified. This change in the output signal contributed to the variation of the noise.

2.4   Monte Carlo simulation

In order to pin-point specific problems, the evaluation of the Hadronic Endcap performance requires the comparison of experimental data with detailed simulations using the Monte Carlo method [9]. A first Monte Carlo package was released in 1996 to study the prototype modules. Since then, several changes have been implemented to the simulations. For example, Monte Carlo events now store additional quantities, such as leakage energy, which are not available in experimental data [10]. In 1999, a new version of the simulation package was released that includes all of the geometry and layout details of the August 1999 beam tests. Simulations are performed for electron and pion beams of different energies, and for different impact points on the calorimeters.
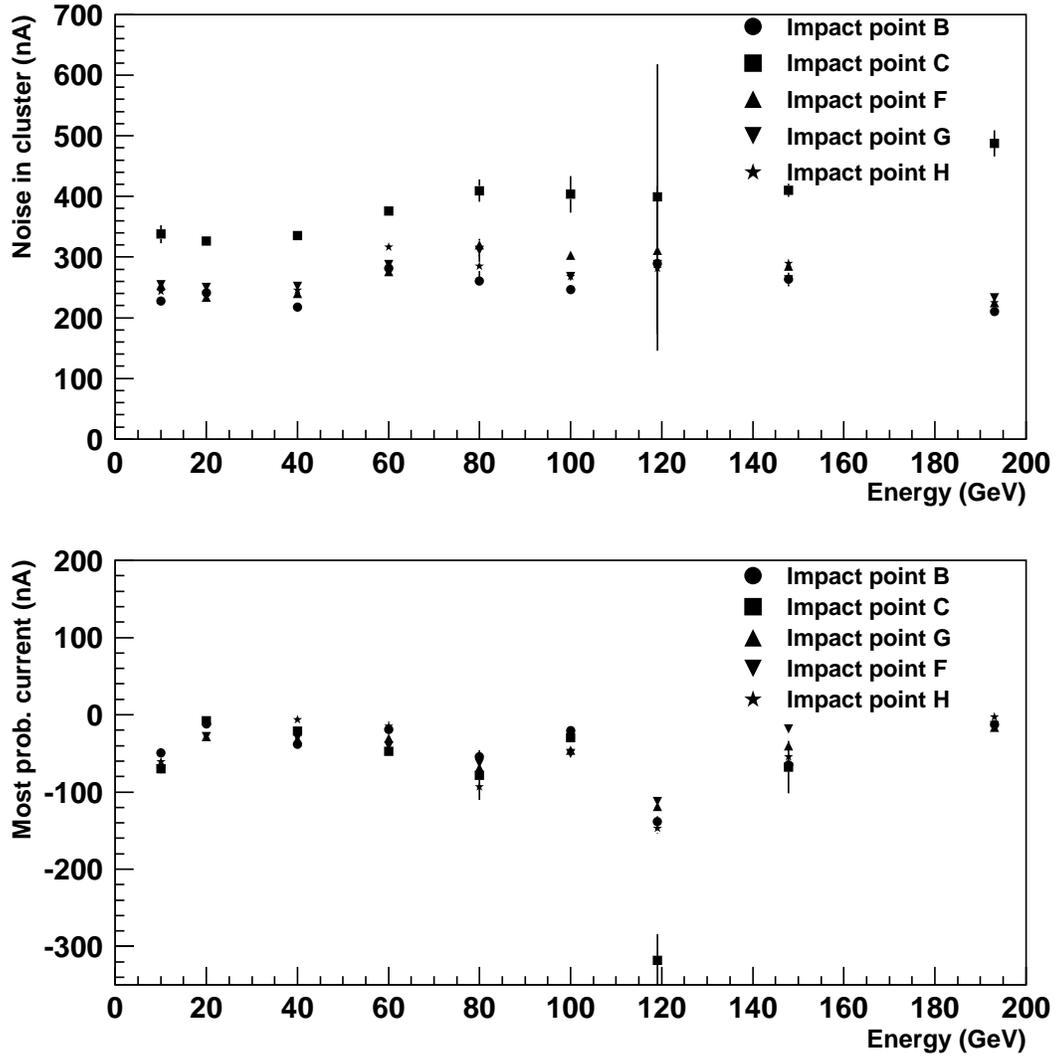
Figure 10: Cluster electronic noise σ and most probable current μ for all the electron runs studied. The clusters are made of 9 readout cells, except for beams at impact point C (12 readout cells). The electronic noise and most probable current are obtained from asymmetric Gaussian fits. The error bars shown include the statistical and systematic errors.
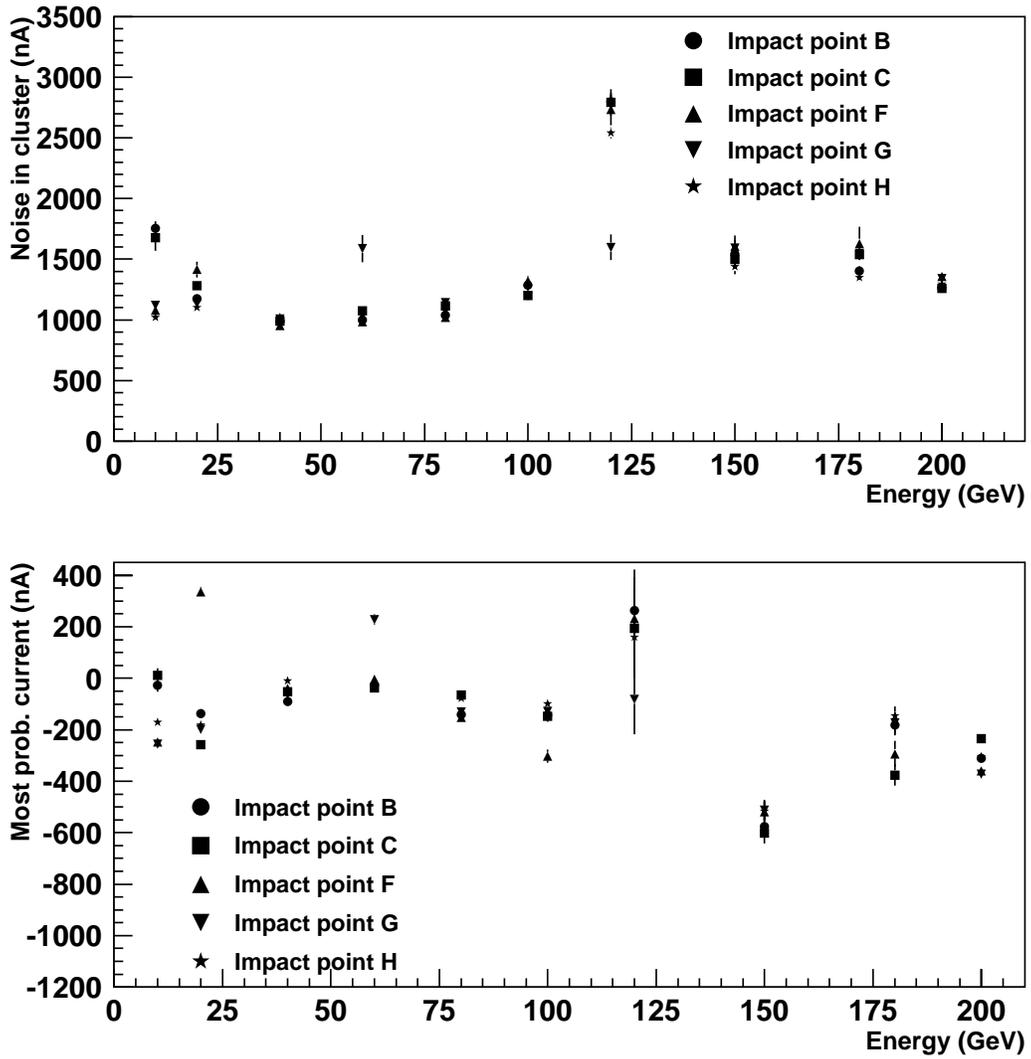
Figure 11: Cluster electronic noise σ and most probable current μ for all the pion runs studied. The clusters are made of 53 (B and C) or 54 (F, G and H) readout cells. The electronic noise and most probable current were obtained from asymmetric Gaussian fits. The error bars shown include the statistical and systematic errors.

2.4.1 Electron simulation

Electron beam events are simulated for two beam locations, corresponding to impact points C and G (see Figure 1). There are no geometrical differences between modules 1, 2 and 3 in the setup of the Monte Carlo, and hence the detector is symmetric about the centre of module 2. Therefore, the results obtained from simulations at points C and G are also used to study the symmetric points B and F. The energies of the electron beam are set to nine different values, between 10 to 193 GeV, corresponding to the ones used in the beam test. For each run, 2000 events are simulated. The analysis procedure consists of three main steps: event selection, energy reconstruction, and parameterization of the resolution.

In the case of simulated electron and pion runs, one and only one hit is required to occur in each plane of MWPCs to prevent an overlap of events. Other software trigger selections are applied and are described elsewhere [11]. Their effect is rather small, affecting less than 1% of the events in a run. On average, 85% of the events pass all the cuts. The events produced are translated to the same format as the one used for the beam test data, so that exactly the same analysis procedure can be followed. The analysis procedure is described in detail in Section 5, and the resolution of the calorimeter obtained from simulations is presented in Section 3.5 together with the electron beam test results.

2.4.2 Pion simulation

Pion beam events are also simulated at impact points C and G using the hadronic simulation package G-CALOR [12]. In the case of pions, each run are made up of 4000 events. The simulations are done for ten different energies, from 10 to 200 GeV, corresponding to the ones used in the beam test. The analysis procedure is the same as for electrons. First, events selection is applied, then the events are translated to a format compatible with the one used for the beam test data. Finally, the events are processed as described in Section 6 so that the hadronic resolution of the calorimeter can be evaluated. The pion resolution obtained from simulated

events and from beam test data are presented in Section 4.4.

3   Analysis of Electron Beam Test Data

In order to study the electromagnetic performance of the Hadronic Endcap Calorimeter, experimental data were taken for different electron beam energies. For each of the selected impact locations, the modules were subjected to electron beams of 10, 20, 40, 60, 80, 100, 119.1, 147.8 and 193.1 GeV. Each run is typically made up of 10,000 events, of which 65% to 92% pass the trigger cuts. The readout cell signal for each event is reconstructed using the digital filtering method (Section 2.2.2), and a cell cluster is formed, as explained in Section 3.2. The linearity of the response and hence the electromagnetic scale α_{em} (Section 3.3) are extracted from the mean signal produced for each beam energy. The constant α_{em} is the factor needed to translate the current (nA) measured in the calorimeter to the incoming particle energy (GeV). Pion contamination of the beams is observed, but its effect on the present analysis is found to be negligible (Section 3.4). To study the intrinsic characteristics of the HEC, the energy resolution is extracted after subtracting the measured electronic noise. Finally, the spatial uniformity of the response of the HEC is surveyed (Section 3.6). The results obtained are compared in each section with the ones obtained in 1998, and with the values from Monte Carlo simulations. Note that the HEC calorimeter is not optimized for the detection of electrons. Indeed, the electromagnetic showers in ATLAS will rarely penetrate through the electromagnetic endcap to reach the HEC. Nonetheless, the performance of the calorimeter to electron beams is crucial because hadronic showers have an intrinsic electromagnetic content, mainly in the form of $\pi^0 \rightarrow \gamma\gamma$. Furthermore, the response to electrons is more precise than for pions, so it is useful to study the electron response to look for unexpected effects such as poor resolution or lack of linearity that might point to detector design problems.

3.1 Trigger cuts

As explained in Section 2.1.2, the trigger system was used to select the events to be recorded, as well as to further refine the event selection offline. After applying the trigger cuts to the electron runs and keeping only the physics events, 6000 to 9200 events remained to be processed in the analysis. Pion events were still present in the electron sample, but as it will be shown in Section 3.4, software cuts were sufficient to eliminate them.

3.2 Clustering

The calorimeter modules are divided in readout cells, each calibrated independently (see Section 2.1.3). The energy deposited by an electromagnetic shower as it propagates through the calorimeter is distributed over several cells. The calorimeter energy associated to the incoming electron is the sum of all the corresponding cell energies. The cluster size and shape are chosen such that the electromagnetic shower is fully contained. Typically, clusters for the electron runs are composed of 9 cells. The cluster size and shape are independent of energy. Figure 12 shows such a cluster, selected for impact point G. An insignificant amount of energy is deposited in the fourth layer, therefore no cells for this layer are in the cluster.
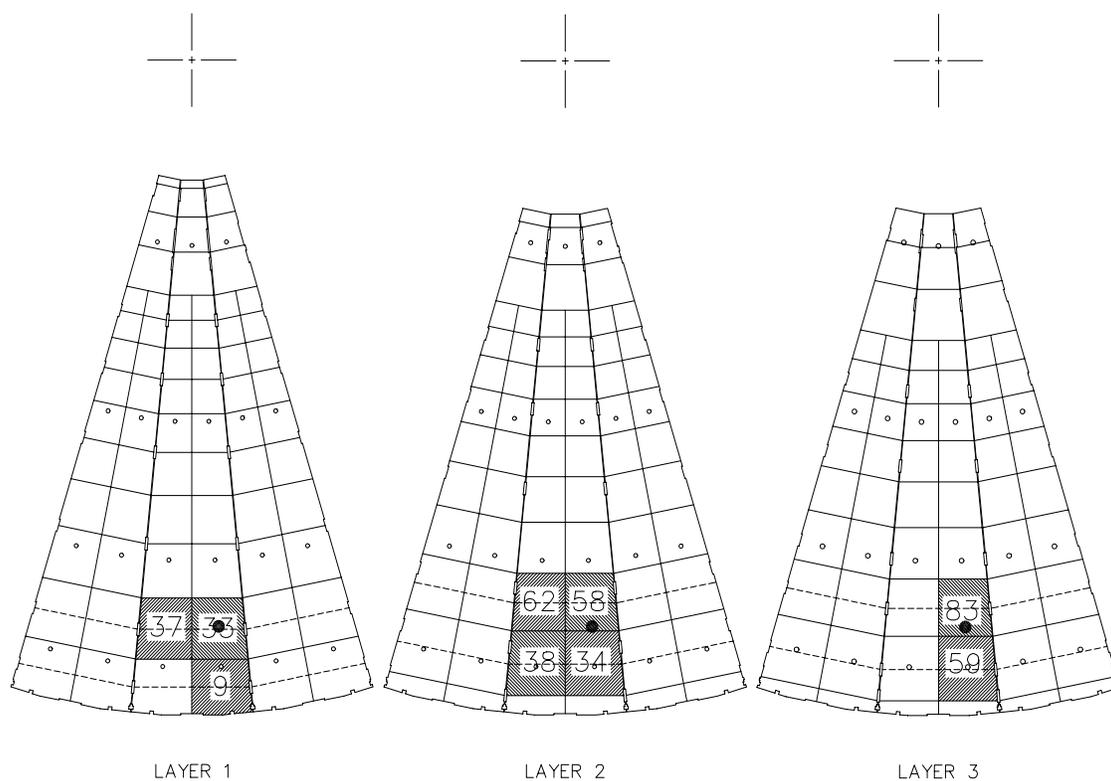
Figure 12: Distribution of a 9 cell cluster designed for electron runs at impact point G. The beam path through the calorimeter is denoted by a bullet. The shaded cells are used in the cluster. The number appearing at the center of each cell corresponds to the readout channel number. No cells from the fourth layer are used. The cross indicates the beam axis during ATLAS operation.

3.3   Response and α_{em} constant

The readout cell response is calculated using the method described in Section 2.2. The response of the HEC is then computed as the difference between the total energy deposited in the cluster and the cluster noise most probable current (observed in the pedestal region, see Section 2.3).

Figure 13 shows the energy deposited (expressed in equivalent nA) in a cluster for different beam energies. In each case, the energy follows the Gaussian distribution as expected. A fit on the region contained between $\pm 2\sigma$ from the mean is also displayed for each histogram. For the 10 and 20 GeV runs, tails are visible on the high energy side of the energy distribution and are caused by high electronic noise, as described in Section 2.3. These tails do not significantly affect the values of the mean (μ_E) and width (σ) of the responses obtained from the Gaussian fits that are used to calculate the electromagnetic constant.

The electromagnetic constant, α_{em}, allows the conversion of energies from nA to GeV for an electromagnetic shower and is expressed as

$$E = \alpha_{em} E(\text{nA}), \tag{1}$$

where E is the reconstructed energy in GeV, and $E(\text{nA})$ is the cluster mean response (after subtracting the cluster noise most probable current, see Appendix B). This constant is evaluated by constructing and minimizing

$$\chi^2 = \sum_i \frac{(E_i - E_{0i})^2}{\sigma_i^2}, \tag{2}$$

where E_{0i} are the beam energies in GeV. The value of α_{em} obtained for all impact points are shown in Table 3.

Figure 14 is a comparative plot showing the ratio between the reconstructed and beam energies. Some discrepancies are observed at energies less than 40 GeV. Nonetheless, most reconstructed energies are within one percent of the beam energies after correcting the cluster response. This correction is done by subtracting the cluster most probable current from the cluster response (see above).
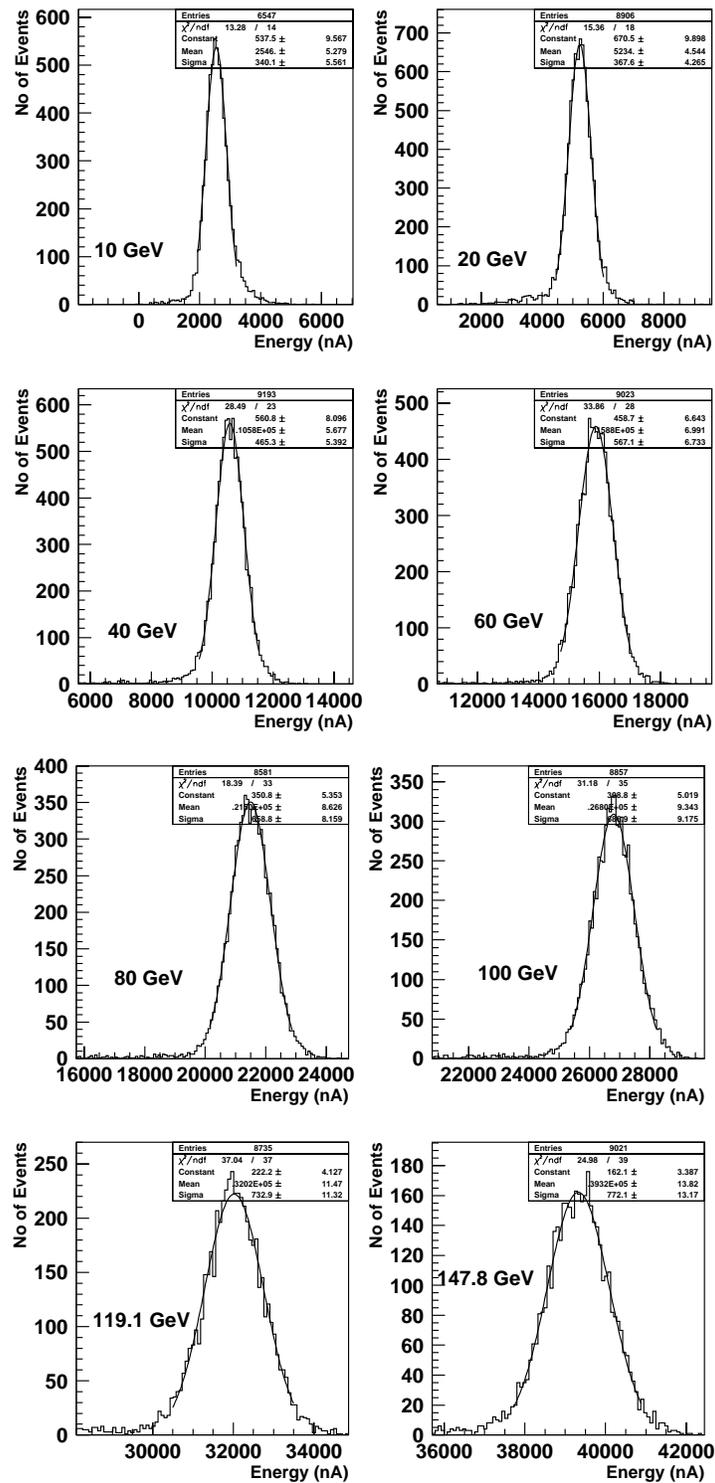
Figure 13: Response of the Hadronic Endcap Calorimeter in units of current measured at impact point G to 10, 20, 40, 60, 80, 100, 119.1, and 147.8 GeV electrons.
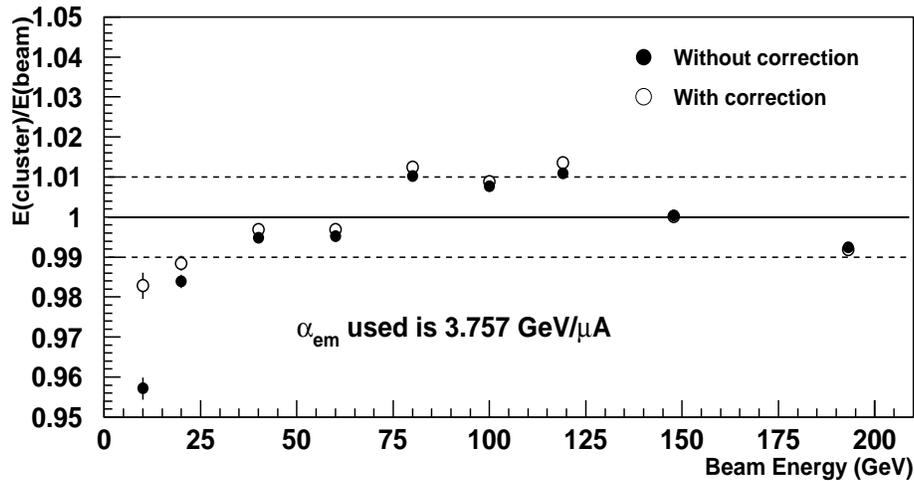
Figure 14: Reconstructed electron energy vs. beam energy at impact point G. The dashed lines represent a 1% variation. The correction on the response (empty circle) was done by subtracting the cluster noise most probable current observed in the pedestal region. This correction improves significantly the linearity of the response at low energy.

In an attempt to improve the linearity of the response, the HEC response to electrons was also parameterized using

$$E = \alpha_{em} \ E(\text{nA}) + b, \tag{3}$$

where b is a constant offset. No significant changes were observed in the reconstructed energy and the offset was found to be consistent with zero. The difference in α_{em} calculated from Equations 1 and 3 was defined as a systematic error. Nonetheless, the systematic error from the observed small non-linearity dominates the final error on α_{em} and is included in the errors shown in Table 3. This error was calculated as the RMS deviation observed in the linearity of the response (Figure 14). Figure 14 shows how the linearity of the response improves when the cluster noise most probable current observed in the pedestal region is subtracted from the response signal.

As can be seen in Table 3, the value of α_{em} is slightly higher at impacts B and C because of the nearness of the beam with the tie-rods at those locations [8]. The

---

[8]The tie-rods are steel rods holding each of the calorimeter modules together. There are 7 of

Impact point	α_{em} (GeV/μA)	Cluster size (# of cells)
B	4.15 ± 0.11	9
C	3.93 ± 0.05	12
F	3.84 ± 0.05	9
G	3.76 ± 0.04	9
H	3.87 ± 0.04	9
Combined (F,G,H)	3.82 ± 0.04	

Table 3: The electromagnetic scale obtained for each of five beam impact positions. The averaged α_{em} comes from the weighted average for impacts F, G, and H only. The observed small non-linearity dominates the final error on α_{em}. Impact points B and C suffer from their nearness with the tie-rods and were not included in the average.

beam is not point like, but has an effective diameter of about (2.5 ± 0.1) cm (see Section 2.1.2). Hence, for some events, a sizeable fraction of the electromagnetic shower energy was deposited in the rods, and the HEC response was thus reduced. The effect of the tie-rods on the response is discussed later in Section 3.6.

The average α_{em} obtained in this analysis is (3.82 ± 0.04) GeV/μA [9], and is different from previous measurements. In fact, measurements of α_{em} in 1998 yielded an average value of 16% less [2]. The electromagnetic constant is determined by the structure of the calorimeter, the liquid argon ionization and the electric field. It should be the same for all modules at all times, independently of the electronics used. It is one of the fundamental measurements which will be of use when the ATLAS detector becomes operational in 2005. This change in the EM scale has caused some concern amongst the HEC group since its origin has not yet been fully understood [10] [6]. It is thought to be due to inadequate calibration procedures before 1999.

them per module, identified by empty circles in Figure 1.

[9] The systematic error from the observed small non-linearity dominates the final error on α_{em}. Hence, the error on the average α_{em} is taken as the average of the errors obtained at each impact point.

[10] Andrei Minaenko calculated a value of $\alpha_{em} \approx 3.95$ GeV/μA using the 1999 data.

3.4   Beam contamination

Excess of events in the low energy tail of the response distributions can be seen in Figure 13, especially in the case of the 147.8 GeV electron beam run. These low energy signals come from pion contamination in the beam. Using the same cluster as for the electrons, the study of pion beam data reveals the energy distribution due to pions in the region where the electron signal lies. Figure 15 shows such distribution obtained from 150 GeV pions, with a fit describing a Gaussian distribution summed with a first degree polynomial:

$$P_\pi(E) = Ae^{-(\frac{E-\mu}{\sqrt{2}\sigma})^2} + mE + b, \tag{4}$$

where E is the measured energy in nA, and m and b are the slope and intercept of the polynomial. Finally, A, μ, and σ are the amplitude, mean and standard deviation of a normal distribution, respectively. This empirical function is found to fit the pion data well.

The response energy distribution, $R(E)$, observed for the 147.8 GeV electron run can now be parameterized as the sum of the energy distribution to the pions $P_\pi(E)$ and electrons $P_e(E)$:

$$R(E) = SP_\pi(E) + P_e(E) \tag{5}$$

where S is a scaling factor applied to the pion energy distribution, and $P_e(E)$ is simply a Gaussian distribution of mean μ and width σ. Figure 16 shows the result obtained after applying this parameterization. The function used to describe the energy distribution agrees with the data. Figure 17 displays again the 147.8 GeV electron beam energy distribution, but the parameterization is performed using the electron distribution $P_e(E)$ only, on a range of $\pm 3\sigma$ around μ.

The results obtained for the mean and width of the electron signal Gaussian distribution are the same using either a $\pm 3\sigma$ Gaussian fit on the electron peak, or a fit using an empirical function describing the pion contamination on the low energy data as well as to the electron peak. The pion contamination of the electron beams is therefore ignored in the analysis.

A = (108 ± 3) events
μ = (26.6 ± 0.3)μA
σ = (3.76 ± 0.18)μA
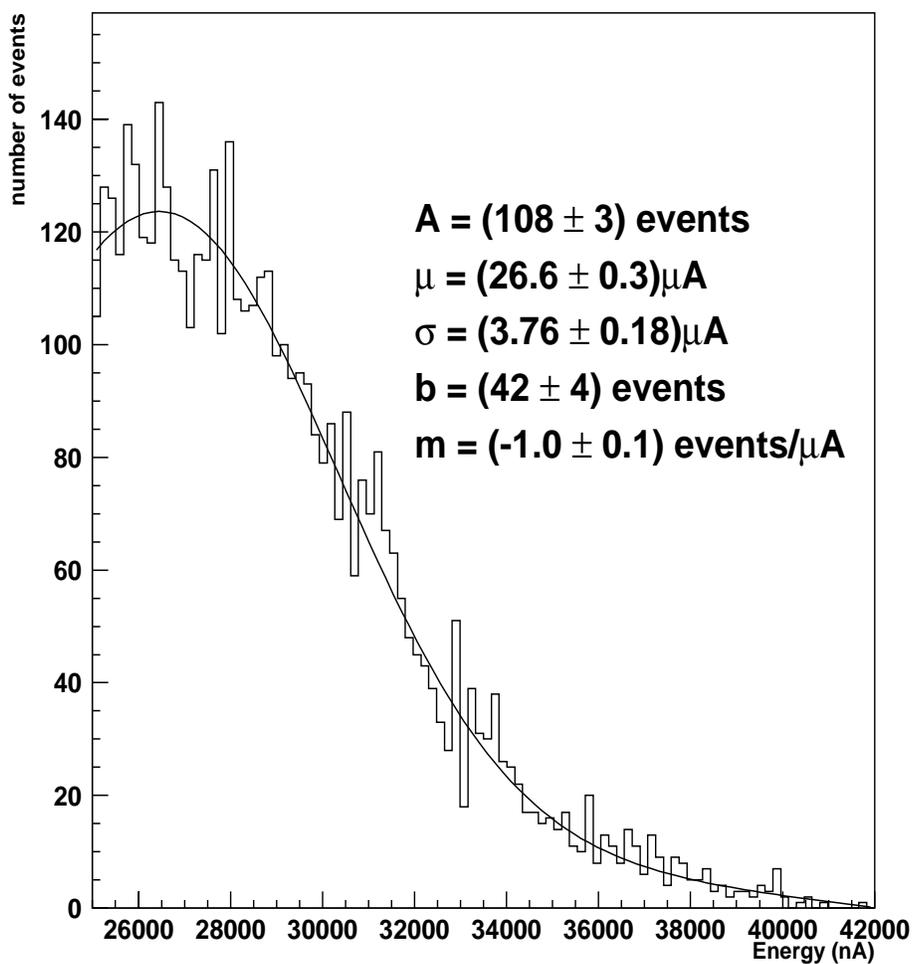b = (42 ± 4) events
m = (-1.0 ± 0.1) events/μA

Figure 15: 150 GeV pion energy distribution using an electron cluster at impact point H. The empirical function used for the fit is a Gaussian (amplitude "A", mean "μ", and width "σ") summed with a first degree polynomial (slope "m", and intercept "b"). $\chi^2/\mathrm{ndf} = 92/88$.
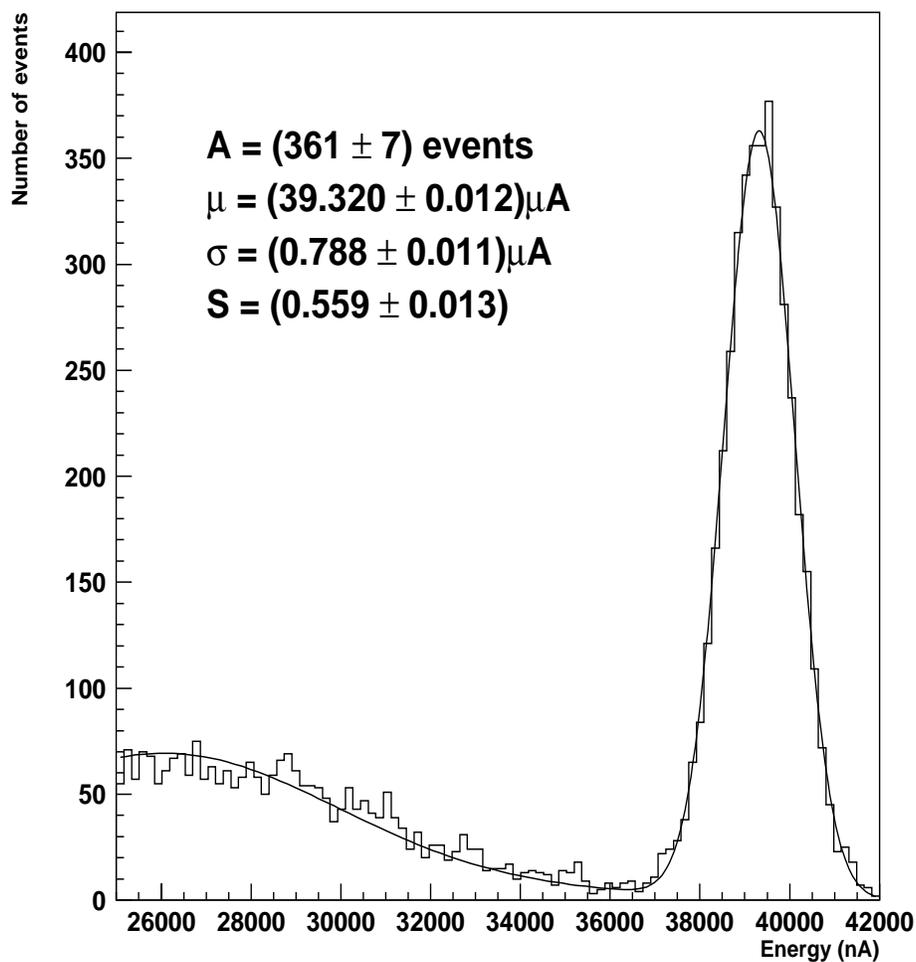
Figure 16: 147.8 GeV electron beam energy distribution. The curve represents a fit for the function describing the pion contamination and the electron signal. The function used for the fit is a Gaussian $P_e(E)$ (amplitude "A", mean "μ", and width "σ"), summed with the pion contamination function $P_\pi(E)$ scaled by a factor "S" (see text). $\chi^2/\text{ndf} = 105/96$.
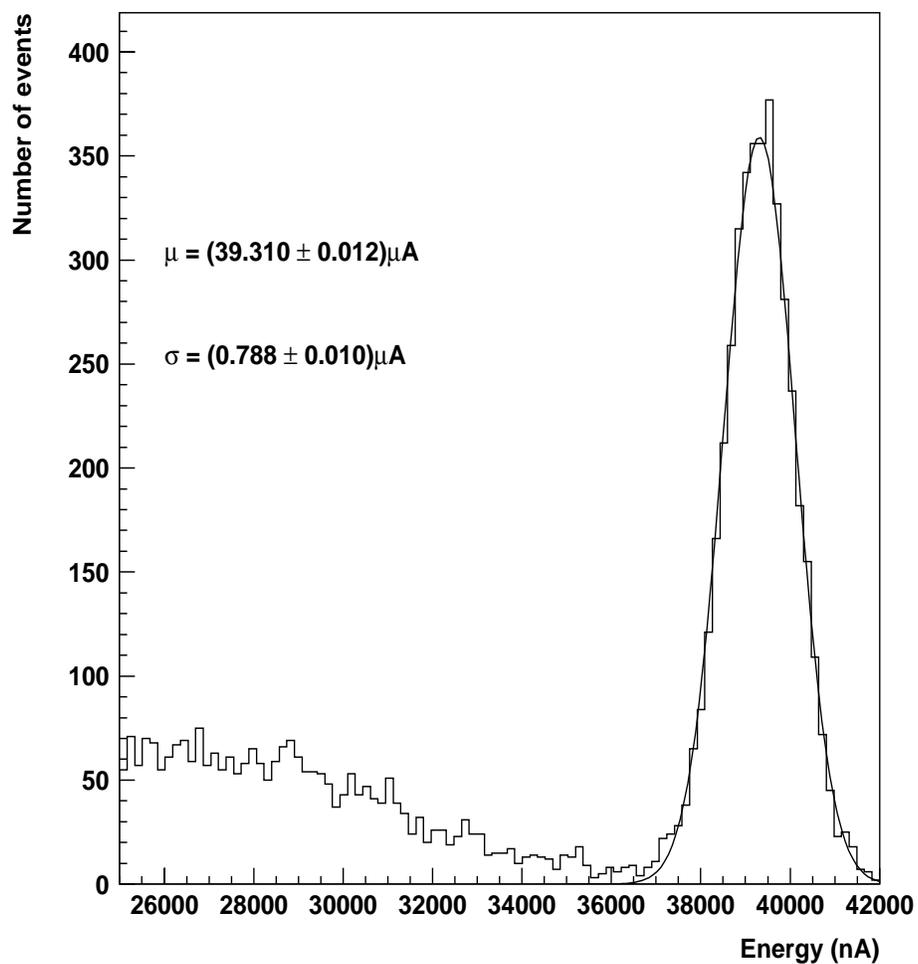
Figure 17: 147.8 GeV electron beam energy distribution with a simple normal distribution fit. The mean, $(39.310\pm0.012)\mu$A, and standard deviation, $(0.788\pm0.010)\mu$A, are within errors of the ones computed with the function describing the pion contamination (see Figure 16).

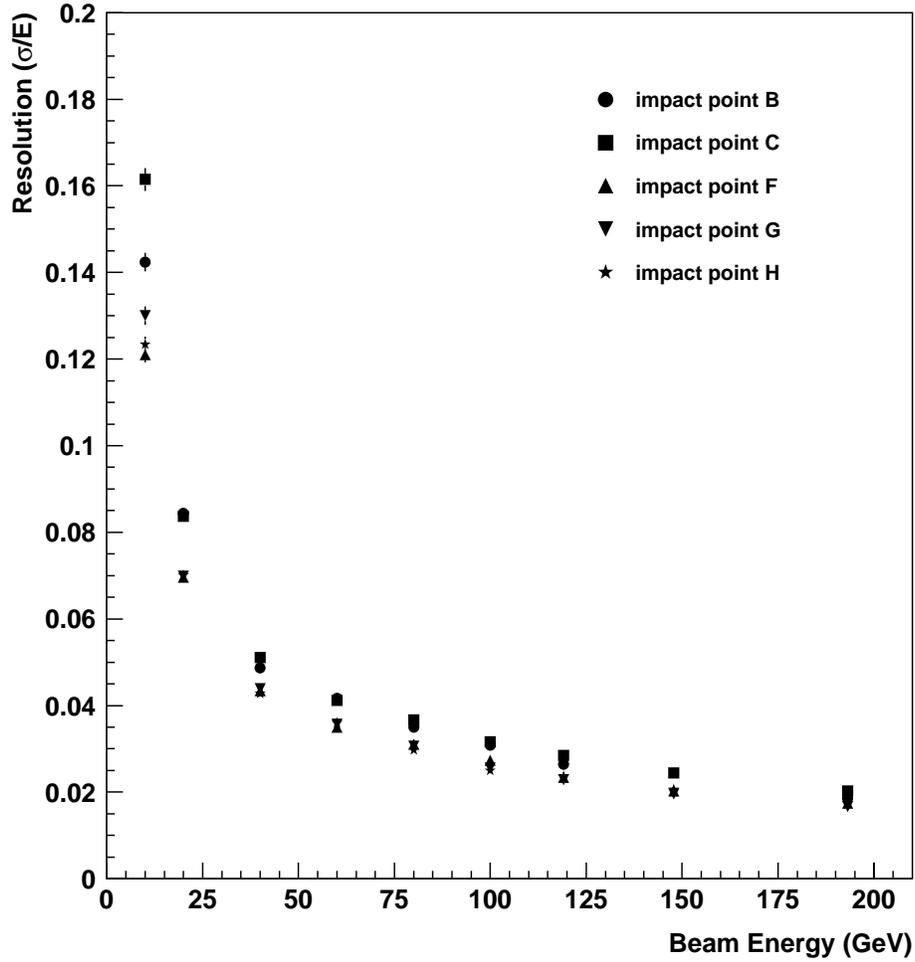Figure 18: Electron energy resolution (σ/E) for all of the studied impact points. The parameters σ and E were obtained from the Gaussian fits performed on the energy distribution (Section 3.3).

3.5 Resolution

In order to evaluate the performance of the HEC, the energy resolution to electrons is studied. The energy resolution, σ/E, is calculated from the width, σ, and response, $E(\text{nA})$, obtained in Section 3.3. Figure 18 summarizes the resolution obtained for every beam energy at the 5 impact points studied. The resolution is worse at B and C due to the nearness of the beam with the tie-rods at those locations [6], causing a loss of energy (see Section 3.3). The effect of the tie-rods on the calorimeter response is examined in Section 3.6.

The energy resolution can then be parameterized as a function of energy as

$$\frac{\sigma}{E} = \frac{A}{\sqrt{E_0}} \oplus B \oplus \frac{C}{E}, \tag{6}$$

where E_0 is the electron initial energy. The parameterization assumes that the electronic noise is constant, but it was observed that the noise, σ_n varied through time, and is therefore different for each energy (see Section 2.3). However, since the electronic noise has been calculated separately, the noise term can be subtracted out in quadrature from the resolution such that only the intrinsic components are left. The intrinsic resolution is then expressed as

$$\frac{\sigma'}{E} = \frac{\sigma \ominus \sigma_n}{E} = \frac{A}{\sqrt{E_0}} \oplus B, \tag{7}$$

where the prime indicates that the electronic noise has been removed. The intrinsic resolution was thus calculated using the values of the electronic noise obtained in Section 2.3. Figure 19 shows the HEC intrinsic energy resolution at the 5 impact points studied as a function of the beam energy. The errors shown include the statistical and systematic errors. Details of the calculation of the intrinsic resolution error are discussed in Appendix B.

The sampling constant A and the constant term B for each impact point are obtained from a fit, and are presented in Table 4. The values of the sampling constant A are consistent for impact points F, G and H, whereas impact points B and C display a worse resolution and sampling term as expected.

A combined fit is made on the overall electron energy resolution and is presented in Figure 20. Only impacts F, G and H are used. The parameterization on the combined average yields

$$\frac{\sigma'}{E} = \frac{(23.29 \pm 0.09)\%}{\sqrt{E_0(\text{GeV})}} \oplus (0.00 \pm 0.13)\%, \qquad \frac{\chi^2}{\text{ndf}} = 23.4/7 \tag{8}$$

This result is incompatible with the values calculated using the April 1998 beam test data [2] [13][11]. The differences are mainly caused by the calibration procedure

---

[11] $\frac{\sigma'}{E} = \frac{(21.5 \pm 0.4)\%}{\sqrt{E_0(\text{GeV})}} \oplus (0.0 \pm 0.4)\%$ (O'Neil), and $\frac{\sigma'}{E} = \frac{(22.0 \pm 0.1)\%}{\sqrt{E_0(\text{GeV})}} \oplus (0.0 \pm 0.2)\%$ (Dobbs et al.).
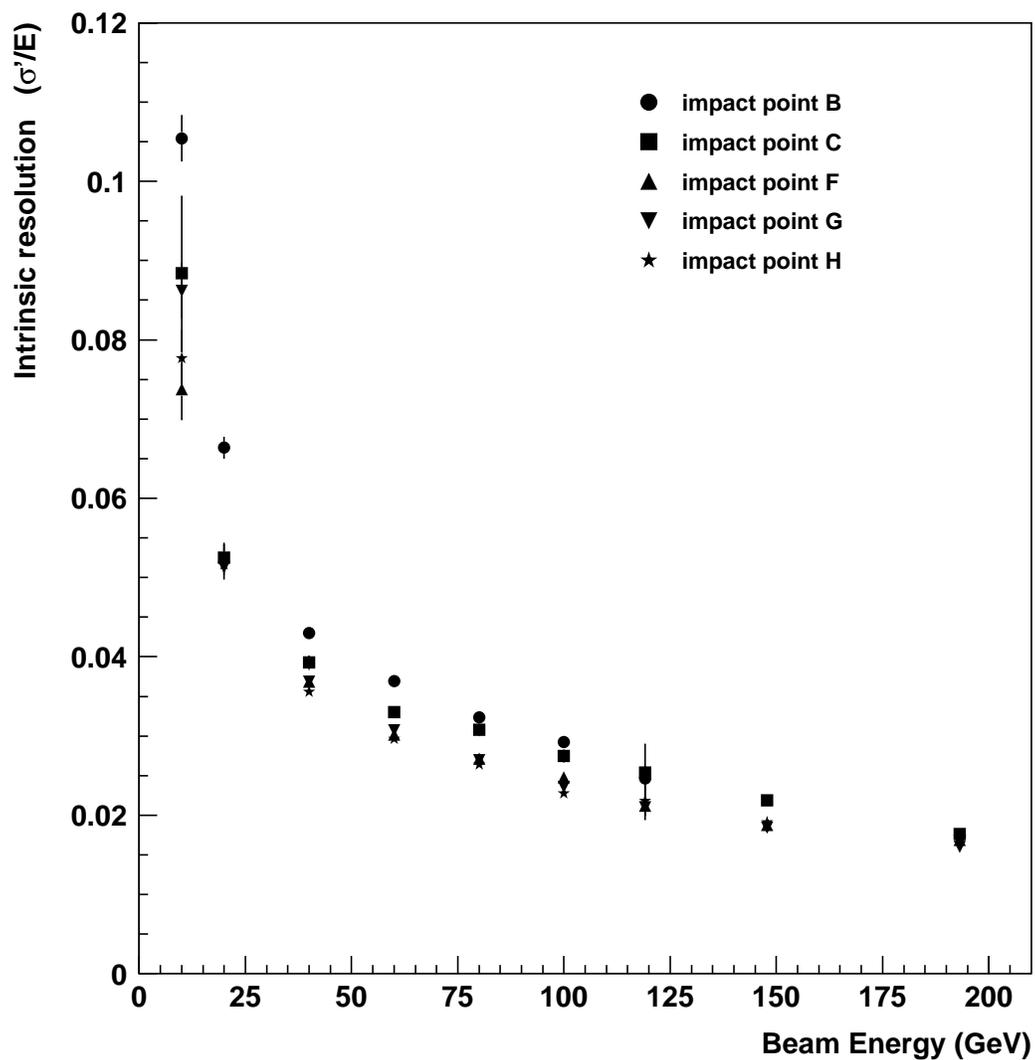
Figure 19: Electron intrinsic energy resolution (electronic noise subtracted) vs beam energy for the 5 impact points studied. The error bars include the statistical and systematic errors.
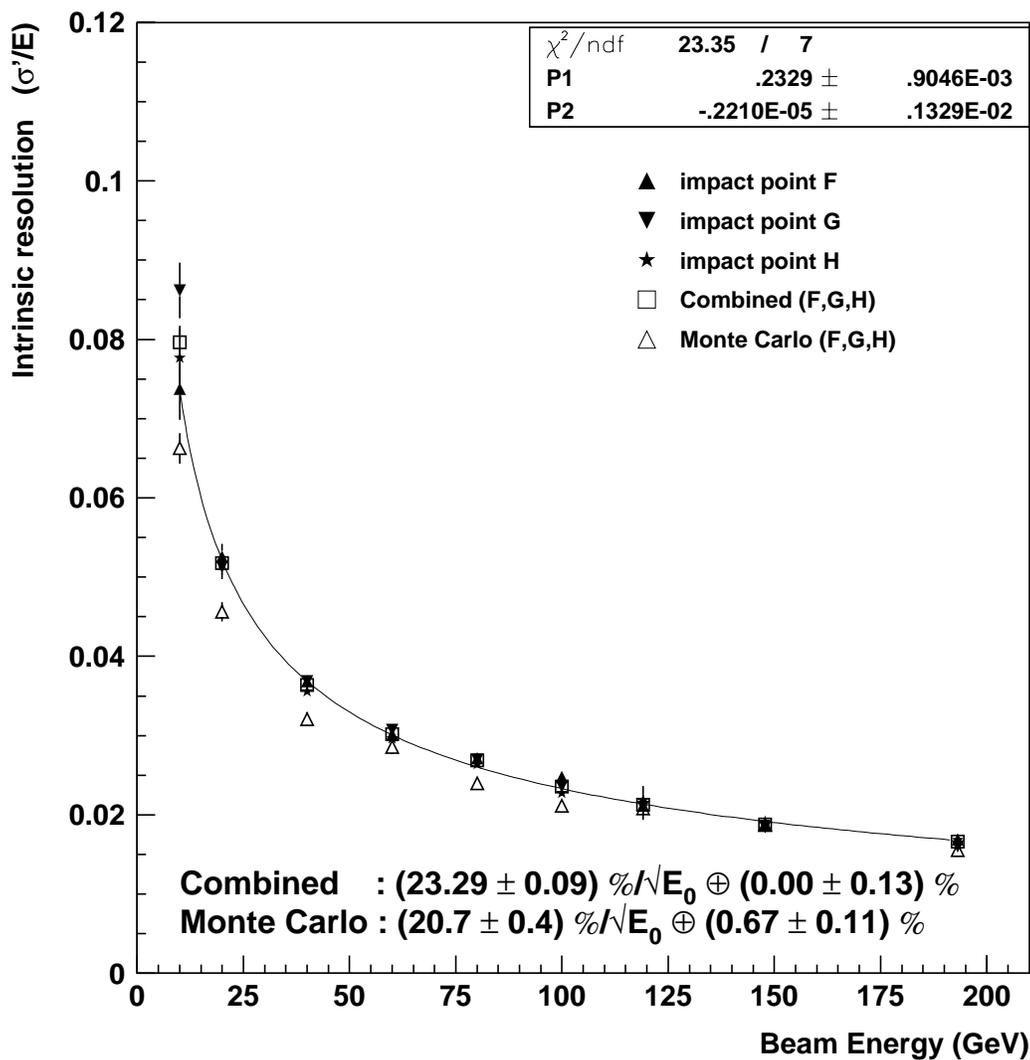
Figure 20: Combined electron intrinsic energy resolution (electronic noise subtracted) vs. beam energy at impact points F, G, and H. The error bars are calculated from the RMS deviation of the resolution at the impact positions F, G, and H. The resolution from Monte Carlo simulations is also displayed.

Impact point	Sampling coef. (A) (%√GeV)	Constant term (B) (%)	χ^2/ndf
B	27.1 ± 0.4	0.00 ± 0.14	56.2/7
C	25.5 ± 0.6	0.2 ± 0.6	27.1/7
F	23.65 ± 0.16	0.0 ± 0.4	13.5/7
G	23.18 ± 0.15	0.0 ± 0.12	33.6/7
H	22.8 ± 0.3	0.36 ± 0.15	6.01/7
Combined (F,G,H)	23.29 ± 0.09	0.00 ± 0.13	23.4/7
Monte Carlo (F,G,H)	20.7 ± 0.4	0.67 ± 0.11	11.0/7

Table 4: Resolution parameters for electrons for the 5 impact points studied. Impact points B and C suffer from their nearness with the tie-rods.

not being adequate in 1999 (Section 2.1.3), which caused the response to be different from one readout cell to another as will be shown in Section 3.6. Furthermore, the treatment of non-Gaussian tails in this analysis may lead to an underestimate of the effective electronic noise.

Monte Carlo electron studies of the calorimeter were also performed for impacts F, G and H and yielded an intrinsic resolution of

$$\frac{\sigma'}{E} = \frac{(20.7 \pm 0.4)\%}{\sqrt{E_0(\text{GeV})}} \oplus (0.67 \pm 0.11)\%, \qquad \frac{\chi^2}{\text{ndf}} = \frac{11.0}{7}. \qquad (9)$$

The intrinsic resolution was obtained directly from σ/E [12] since neither electronic noise nor cell miscalibration were simulated in the Monte Carlo. The latter mainly accounts for the discrepancies between the Monte Carlo and the beam test data results.

3.6   Uniformity

Another point of interest for electron data is the uniformity of the response of the calorimeter. How does the response vary when electrons impinge on the calorimeter between two cells, or near a tie-rod ? To answer these questions, horizontal (X) and vertical (Y) scans with 147.8 GeV electron beams were performed. These scans are a collection of runs where the impact point of the beam is changed by steps of

---

[12] $\sigma/E = \sigma'/E$ for Monte Carlo simulations

10.0 mm. Using the multi-wires proportional chambers (MWPCs), it is possible to know where each electron enters the calorimeter. Figure 21 shows how the relative response (energy reconstructed using the average α_{em} over the energy of the beam) varies with the impact point as the electron beam moves from cell 33 to cell 37. X = -5.1 mm is located between cells 33 and 37, in the central module (see Figure 12) and is plotted in Figure 21 as a vertical line. The difference in response comes mainly from the miscalibration of cells 33 relative to cell 37, where most of the electron energy is measured, as shown in Figure 22. The range in the difference of the response is around 2.4%. This change in the response agrees with the 2.3% difference between the electromagnetic scales computed for impact points G and F (see Table 3) which correspond to a beam centered on cells 33 and 37, respectively.

A vertical scan with a 147.8 GeV electron beam was also made in the same manner described above, between locations corresponding to the area covered by cells 33 and 57 (impact points G and C). Using this scan, the effect of the tie-rods in the response of the calorimeter is studied. Figure 23 shows how the response behaves as electrons approach a tie-rod. The tie-rod is located in cell 57, as shown in Figure 1, at about Y = 16.0 cm. The response starts dropping dramatically around Y = 14.0 cm (the location of impact point C is at Y = 13.4 cm) and goes down by nearly 20% at the tie-rod. Since the beam has a radius of about 1.25 cm (see Section 2.1.2), some of the electrons for a beam collimated at impact C are within the effective drop-off range of the tie-rod. This effect explains why α_{em} is higher for impact points B and C than for the three other impact points (see Table 3). It is also the reason why the resolution and the sampling constant term at points B and C are larger than the value obtained by the combined fit.

From previous beam test analyses, the problems encountered in the uniformity of the response of the calorimeter to electrons are understood to be due to cell miscalibration. This affects the calculation of α_{em} and the resolution. The presence of tie-rods near impact points B and C has an even greater effect on the response of the calorimeter. But this effect is purely caused by setup of the beam tests. In fact,
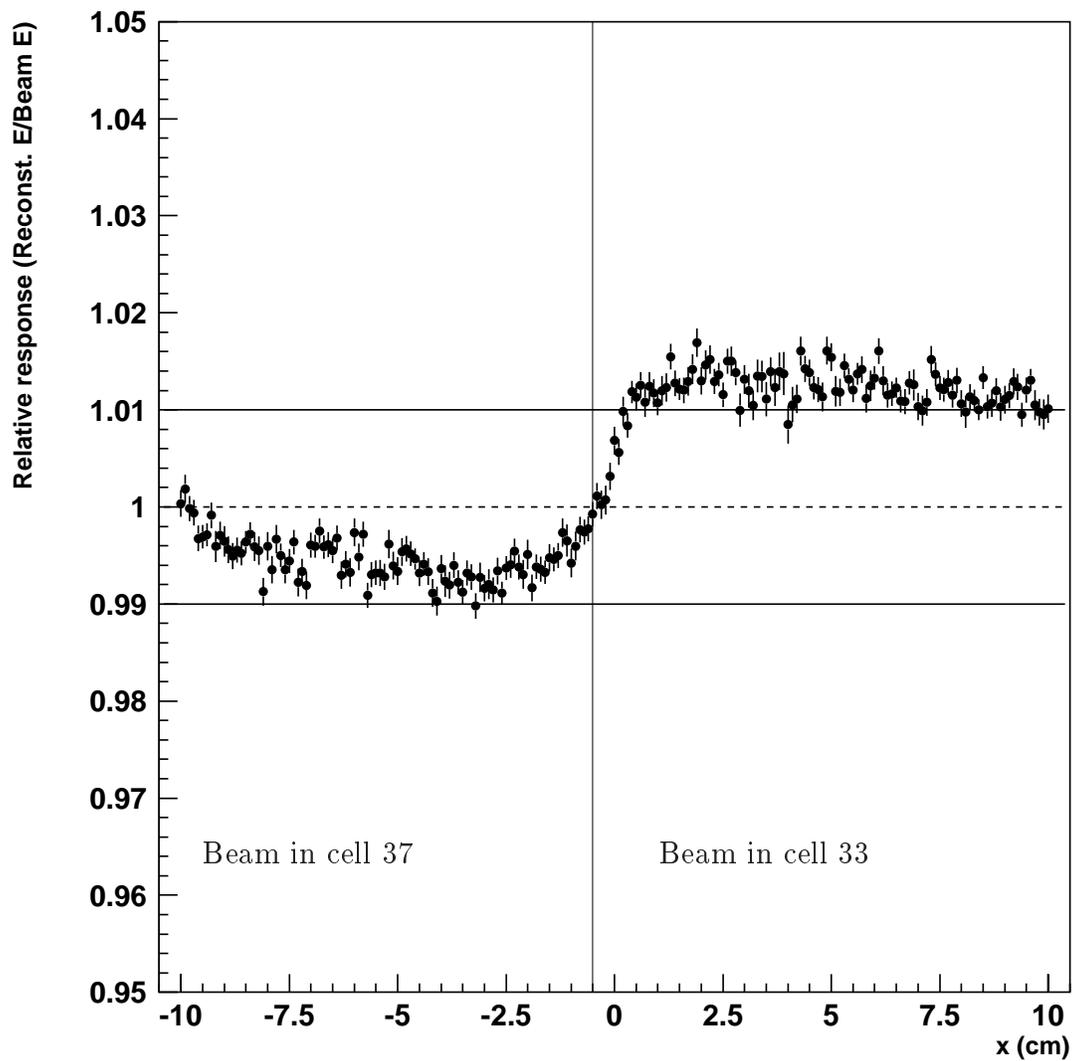
Figure 21: Relative response of the calorimeter vs. beam location for 147.8 GeV electrons. The cluster selected for reconstruction was the same for all events and all positions. The error bars shown are purely statistical. Y = -39 mm.
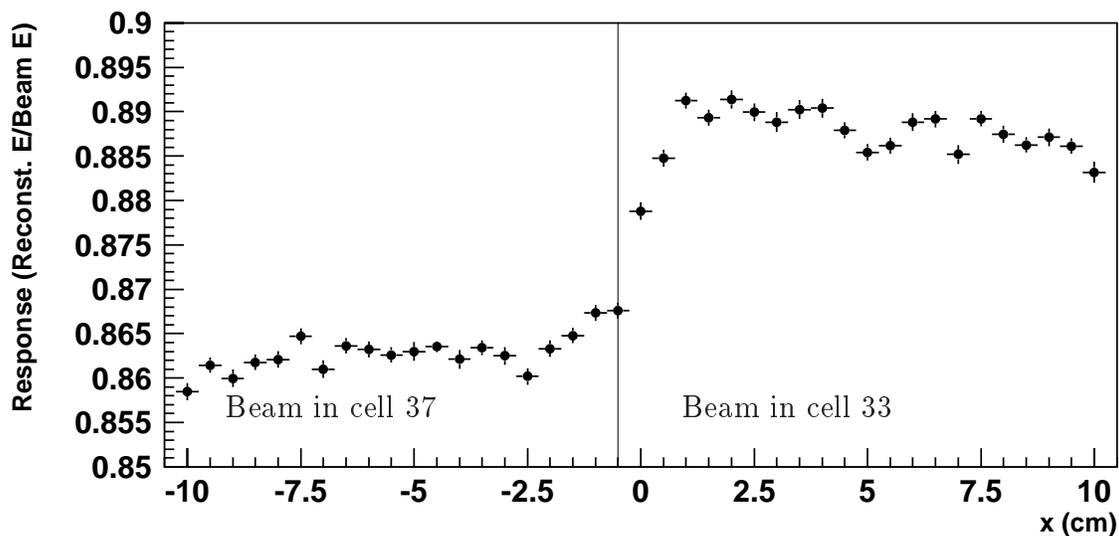
Figure 22: Relative response from cells 33 and 37 vs. Beam location for 147.8 GeV electrons. The response is the sum of the signal from cells 33 and 37 only. The difference between the signal across the symmetry axis (X = -5.1 mm) is about 2.4%. The error bars shown are purely statistical.

in ATLAS particles will not come in a direction parallel to the rods (see Figure 2), but at an angle. Furthermore, electrons and photons will be mainly contained in the electromagnetic calorimeter such that mainly hadronic showers will deposit energy in the HEC. Therefore, a much smaller fraction of the total shower energy will be 'lost' in the tie-rods.
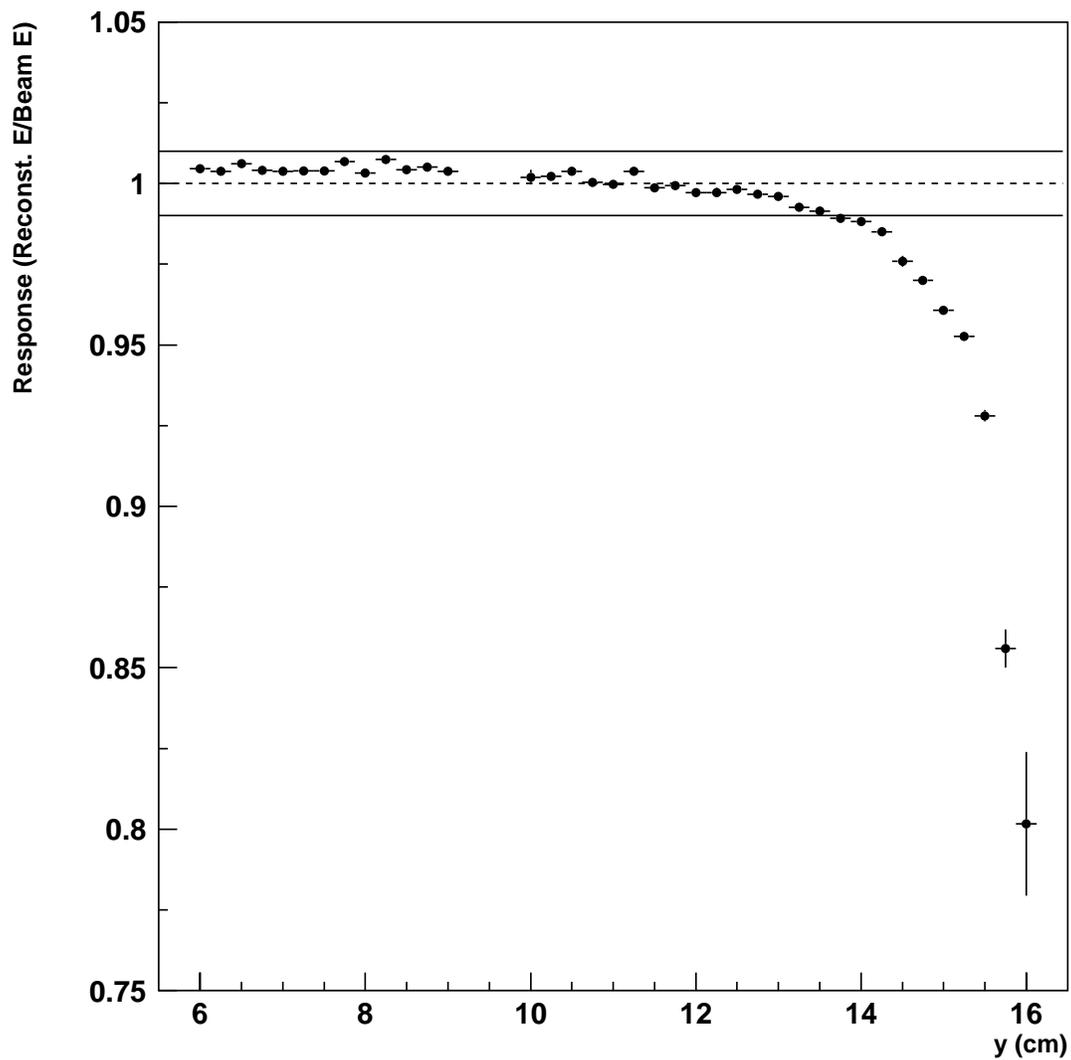
Figure 23: Response of the calorimeter vs. beam impact for 147.8 GeV electrons. The cluster selected for reconstruction is the same for all events and all positions. The error bars shown are purely statistical. X = 80 mm. Note how the response drops as the electrons are getting closer to the tie-rod (Y = 16.0 cm).

4   Analysis of Pion Beam Test Data

The intrinsic performance of the Hadronic Encap Calorimeter to hadrons is determined by studying the response and resolution of the calorimeter to pions. For each of the selected impact locations, the modules were subjected to pion beams of 10, 20, 40, 60, 80, 100, 120, 150, 180, and 200 GeV. Each run is typically made up of 10,000 events, of which 25% to 90% pass the trigger cuts. The readout cell signal for each event is reconstructed using the digital filtering method (Section 2.2.2). Because of the different nature of the processes involved in hadronic showers, larger clusters were used to achieve full or nearly full containment of the showers. The response and the intrinsic energy resolution of the HEC to pions is presented in this section and the resolution is compared with the values obtained from Monte Carlo simulations. Finally, the electromagnetic to hadronic response ratio, e/h, is evaluated.

4.1   Trigger cuts

In order to remove impurities from the pion sample, the triggers presented in Section 2.1.2 were applied and include a physics trigger requirement (pre-trigger), and a pile-up and random veto. Again, the limitation of the Cherenkov detector to low energies prevented its use in eliminating electron impurities from the beam. Nonetheless, software cuts were sufficient to remove electrons from the pion data sample. Muon events were removed by using the muon trigger, but some impurities were observed for low energy runs. The number of pion events satisfying the above cuts ranged from about 2600 to 9200 events for all of the runs.

4.2   Clustering

Full or nearly full containment of the hadronic showers has to be achieved in order to study the intrinsic properties of the calorimeter. Hence, 54 cells clusters are used to reconstruct the energy of the pions. Figure 24 displays the distribution of the cells for such a cluster, selected for impact point G. In the case of impact points

B and F, 53 cells clusters are used because of a dead ADC channel (cell 91) in the 3rd depth. The clusters used for pion data analysis are much larger than the ones used for electron runs because the hadronic showers are developing much further in the detector and are much broader. The down side of using these large clusters is that the total electronic noise is much greater than the one in electron clusters (see Section 2.3).

4.3 Response

In order to calculate the response of the HEC to pions, the procedure described in Section 2.2 is used. As for the electron analysis (Section 3.3), the response of the HEC to pion is then corrected by subtracting the cluster noise most probable current from the cluster signal (observed in the pedestal region, see Section 2.3). This correction increases the response significantly at low energy, as it was shown in Figure 14.

Figure 25 shows the energy deposited (expressed in equivalent nA) in a cluster for 10 to 150 GeV pion beam. Muon events can be seen for beams of intermediate energy (peak centered near 0 GeV). Non-Gaussian tails are also present on the high energy side of the energy distribution and are caused by high electronic noise as discussed in Section 2.3. These tails do not significantly affect the values of the mean (μ_E) and width (σ) of the pion response obtained from Gaussian fits. These fits are performed on a region contained between $\pm 2\sigma$ from the mean. For the 10 and 20 GeV pion beams, the fits are done from -1.75σ to +2σ to avoid muon contamination.

Since the HEC is non-compensating, the response to hadrons is not linear, but increases with energy [13]. This phenomenon was described in [14] and can be observed in Figure 26. The left axis on Figure 26 shows the pion response after subtracting the cluster noise most probable current, E(nA) (or π), plotted on an electromag-

---

[13] $f_{\pi^0} = 0.11 \ln E$(GeV), such that the shower electromagnetic content and hence the response increase with energy.
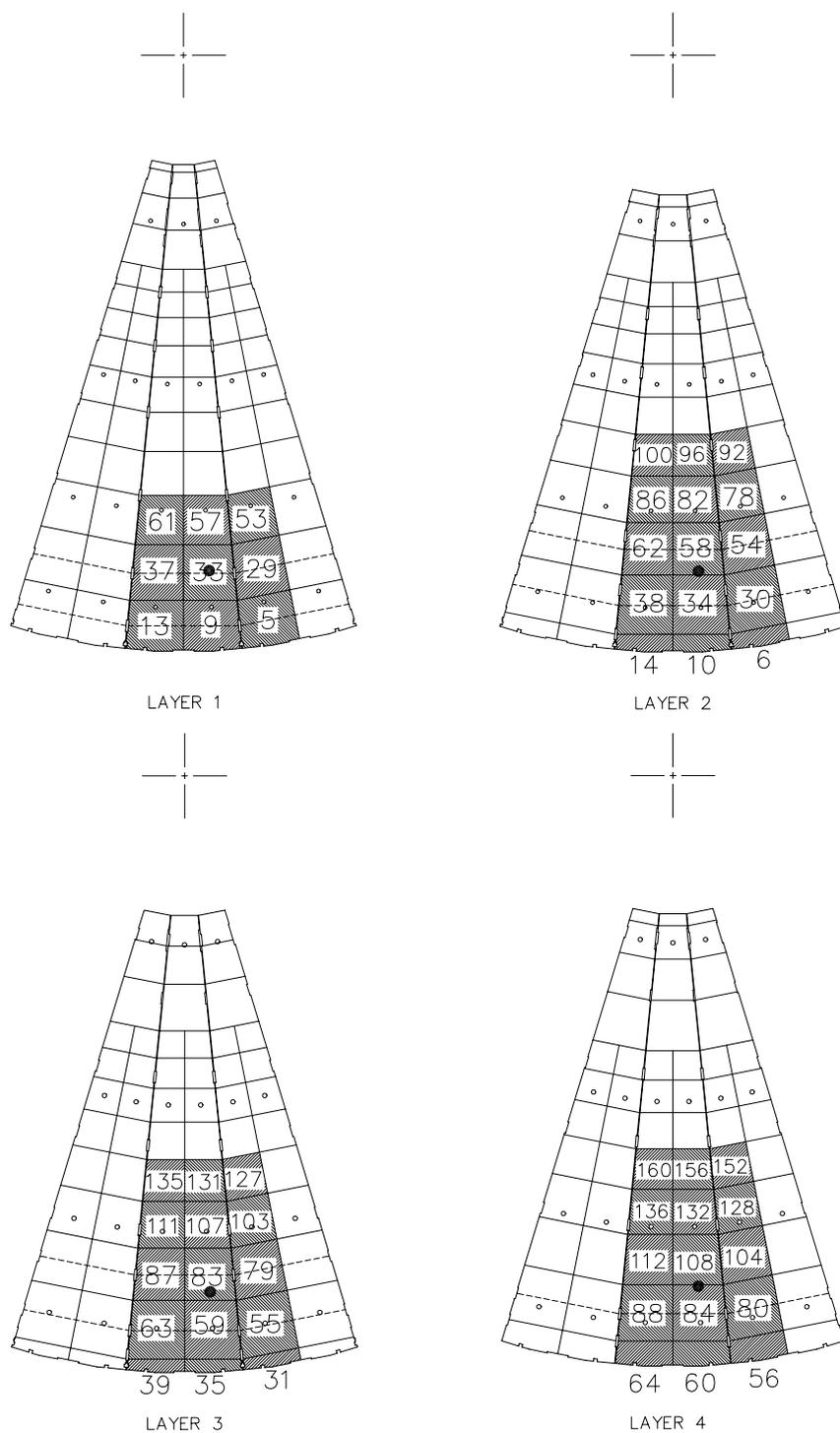
Figure 24: Distribution of a 54 cell cluster designed for pion runs at impact point G. The beam path through the calorimeter is denoted by a black dot. The shaded cells are cells used in the cluster. The number appearing at the center of each cell corresponds to the readout channel number.
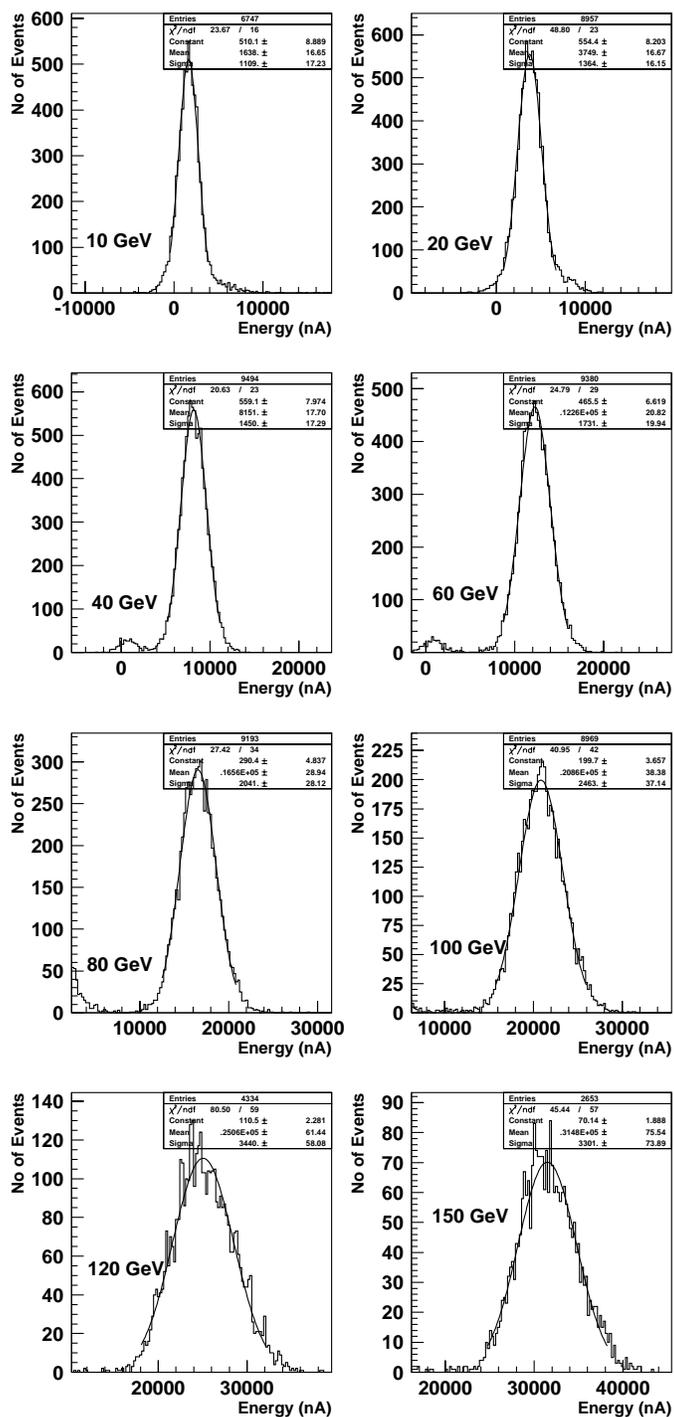
Figure 25: Response of the HEC to pion beams in units of current measured at impact point G for 10, 20, 40, 60, 80, 100, 120 and 150 GeV. A Gaussian fit was performed on a region between $\pm 2\sigma$ of the most probable signal for runs with beam energy greater than 20 GeV, and from -1.75σ to +2σ for the 10 and 20 GeV beams.

netic scale [14], which contains information about the degree of non-compensation of the calorimeter. The values of α_{em} at each impact position (Table 3) are used to reconstruct the pion energy, which reduces calibration problems. On the right axis, the response using the pion scale is shown.

Even though the calorimeter provides good longitudinal containment of hadronic showers, Monte Carlo studies show that there is some leakage of energy, mainly at the bottom of the calorimeter. The total energy loss is about $(3.2 \pm 0.5)\%$ [15].

---

[14]In other words, the response is calculated as $\alpha_{em}\pi/E_0$.
[15]This value is independent of the beam energy, and is in agreement with previous results [15].
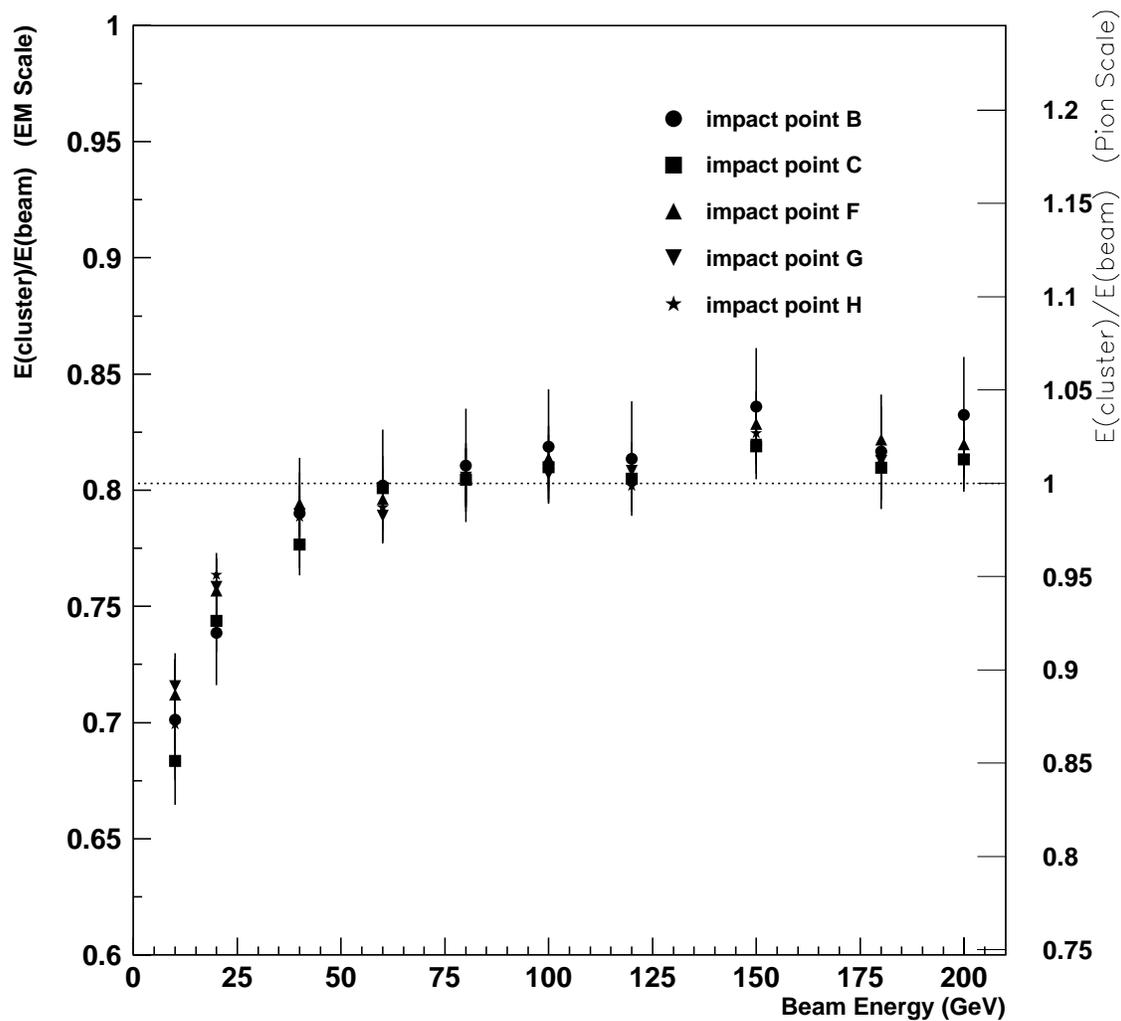
Figure 26: HEC response to pion vs. beam energy using the electromagnetic scale (left) and pion scale (right). The electromagnetic scale factors are presented in Tables 3. The pion scale, which allows one to convert the pion cluster energy from nA to GeV, is calculated using Equations 3.1 and 3.2 applied to pion data. The latter scale is only an approximation since the calorimeter response to pion is not linear.
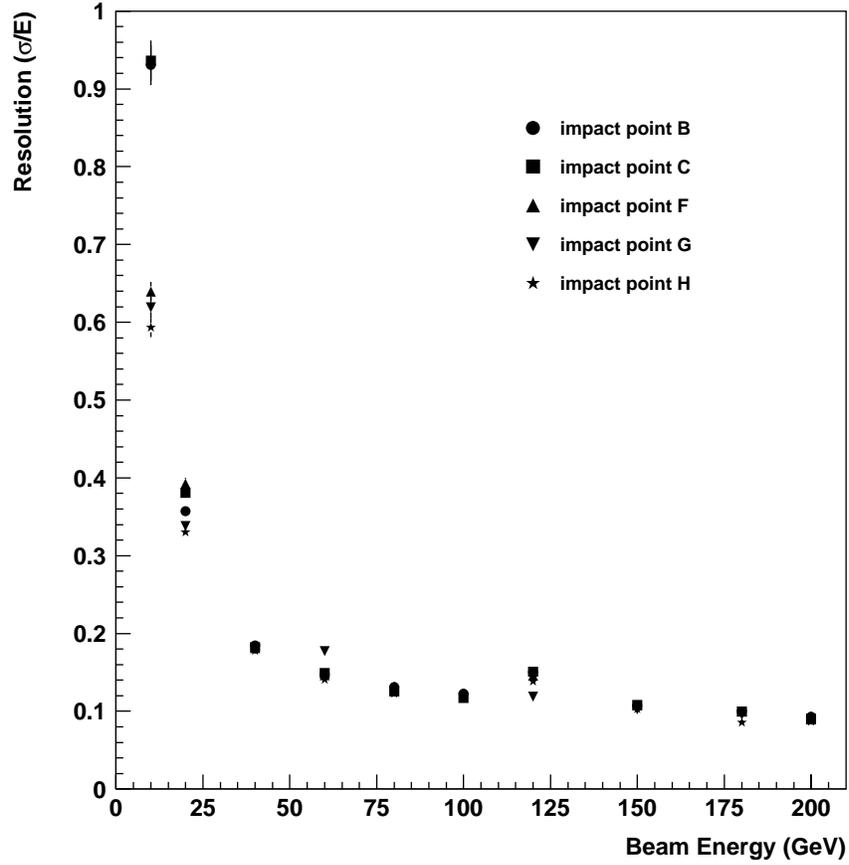
Figure 27: Pion energy resolution vs. beam energy for the 5 impact points studied. The error bars include the statistic and systematic errors. The parameters σ and E were obtained from the Gaussian fits performed on the energy distribution.

4.4 Resolution

The performance of the calorimeter is also assessed in terms of the HEC energy resolution to pions. The energy resolution is calculated using the values of σ and $E(\text{nA})$ [16] obtained in the previous section (Section 4.3). Figure 27 displays the resolution obtained for every beam energy at each of the 5 impact points studied. The resolution is shown to be consistent for impact points B and C, and for impact points F, G and H.

As discussed previously in Section 3.5, the electronic noise can be subtracted out

---

[16] $E(\text{nA})$ is the response of the calorimeter after subtracting the cluster noise most probable current, as described in Appendix B.

in quadrature from the resolution. By doing so, only the intrinsic components of the resolution are left and the parameterization reduces to the expression presented in Equation 7. The intrinsic resolution was thus calculated using the values of the cluster electronic noise obtained in Section 2.3. Figure 28 shows the HEC intrinsic energy resolution at the 5 impact points studied as a function of beam energy. The errors shown include the statistical and systematic errors. Details of the calculation of the intrinsic resolution error are reviewed in Appendix B.

The sampling constant A and the constant term B for each impact point are obtained from a fit, and are presented in Table 5. The values of the sampling constant A are consistent for impacts B and C, and for impacts F and G, whereas impact point H displays a better resolution.

As it can be seen in Table 5, the resolution obtained in beam test for each impact point is worse than the resolution obtained by Monte Carlo simulations using G-CALOR. This may be due again to the electronic noise and cell miscalibration not being included in the simulations. The latter mainly accounts for the discrepancies between the Monte Carlo and the beam test data results. It was also shown previously that hadronic simulations overestimated the calorimeter response, and hence produced a better resolution [15].

Combined fits are performed using the weighted average resolution for each energy for impacts B and C, and F, G, and H. The results obtained are shown in Figures 29 and 30 respectively. The overall combined average parameterization of the resolution obtained from experimental data is

$$\frac{\sigma'}{E} = \frac{(76.2 \pm 0.9)\%}{\sqrt{E_0(\text{GeV})}} \oplus (6.68 \pm 0.09)\%. \qquad \frac{\chi^2}{\text{ndf}} = 15.37/8 \qquad (10)$$

The sampling constant A is compatible with the value obtained in 1998 [17] [13], but the constant term B is 33% larger than previously. This difference in the constant term is mainly caused by the calibration procedure not being adequate in 1999 (Section 2.1.3). Moreover, the treatment of non-Gaussian tails in this analysis may

---

[17] $\frac{\sigma'}{E} = \frac{(78 \pm 2)\%}{\sqrt{E_0(\text{GeV})}} \oplus (5.0 \pm 0.3)\%.$
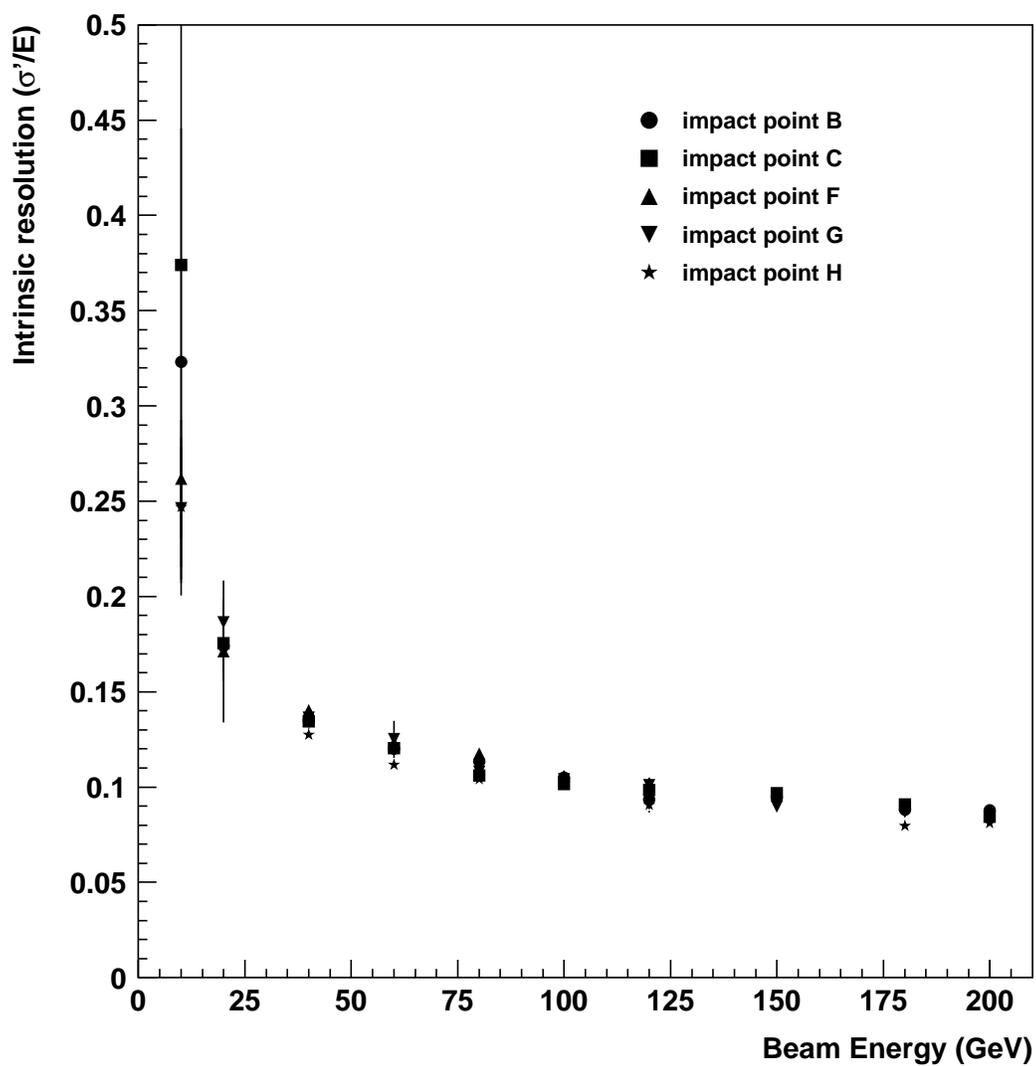
Figure 28: Pion intrinsic energy resolution vs. beam energy at the 5 impact points studied. The error bars shown include the statistical and systematic errors.

Impact point	Sampling coef. (A) ($\%\sqrt{\mathrm{GeV}}$)	Constant term (B) (%)	χ^2/ndf
B	76 ± 2	7.0 ± 0.2	$6.42/8$
C	76 ± 2	6.7 ± 0.2	$9.08/8$
Combined (B,C)	75.6 ± 1.5	6.85 ± 0.15	$7.57/8$
Monte Carlo (B,C)	64.5 ± 0.8	5.51 ± 0.10	$17.1/8$
F	80 ± 2	6.8 ± 0.2	$8.06/8$
G	77 ± 2	6.6 ± 0.2	$4.47/8$
H	72 ± 2	6.4 ± 0.2	$16.6/8$
Combined (F,G,H)	76.6 ± 1.2	6.57 ± 0.12	$12.7/8$
Monte Carlo (F,G,H)	65.7 ± 0.9	5.87 ± 0.11	$9.03/8$
Combined (B,C,F,G,H)	76.2 ± 0.9	6.68 ± 0.09	$15.4/8$

Table 5: Resolution parameters obtained for $\pi^{\pm}$ beams for the 5 impact points studied. The combined average for the calorimeter is given. The corresponding Monte Carlo results are also presented. The line is the fit to the experimental data.

lead to an underestimate of the effective electronic noise. Another analysis [6] also yielded a larger constant term for 1999 [18].

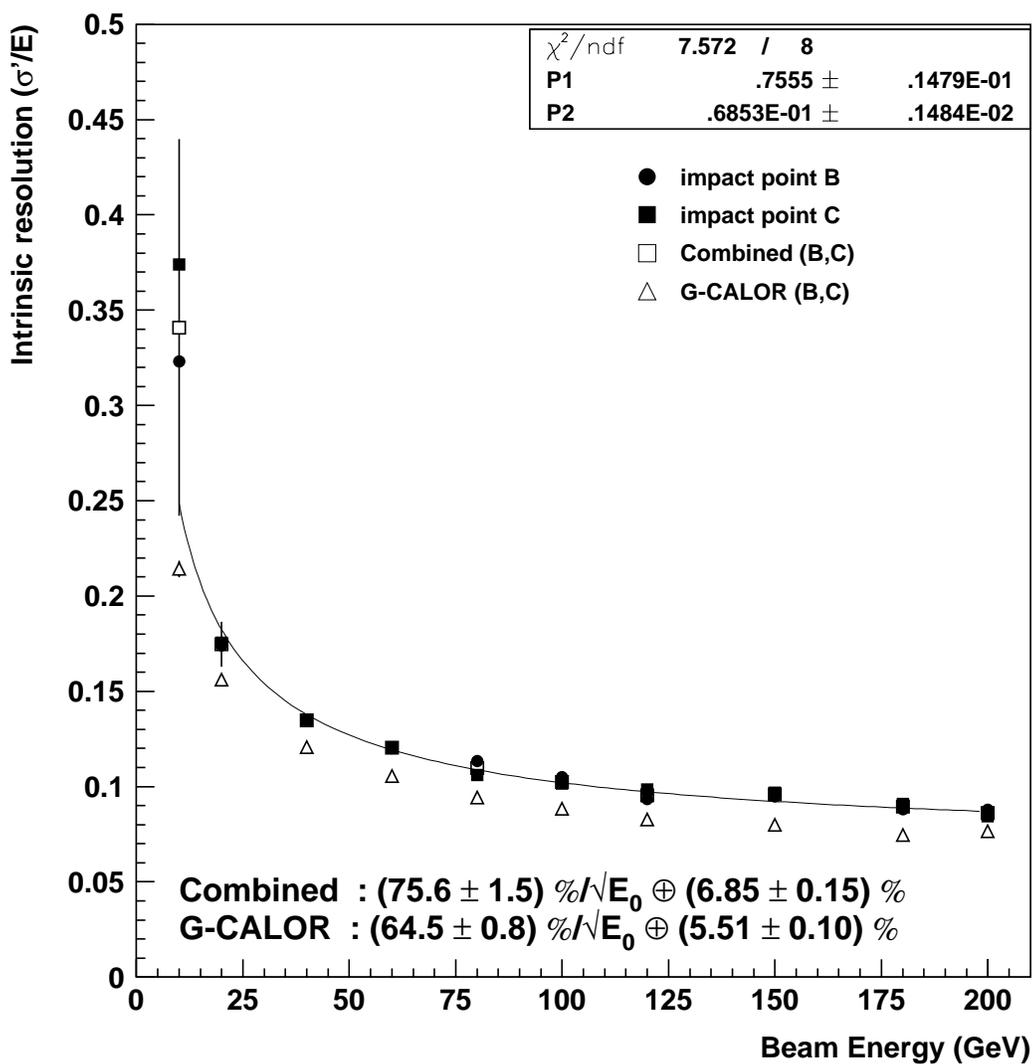[18] $\frac{\sigma'}{E} \approx \frac{75\%}{\sqrt{E_0(\mathrm{GeV})}} \oplus 6\%$.

Figure 29: Combined pion intrinsic energy resolution vs. beam energy at impact points B and C. The error bars were calculated from the RMS deviation of the resolution at impact points B and C. The resolution from Monte Carlo (G-CALOR) is also displayed. The line is the fit to the experimental data.
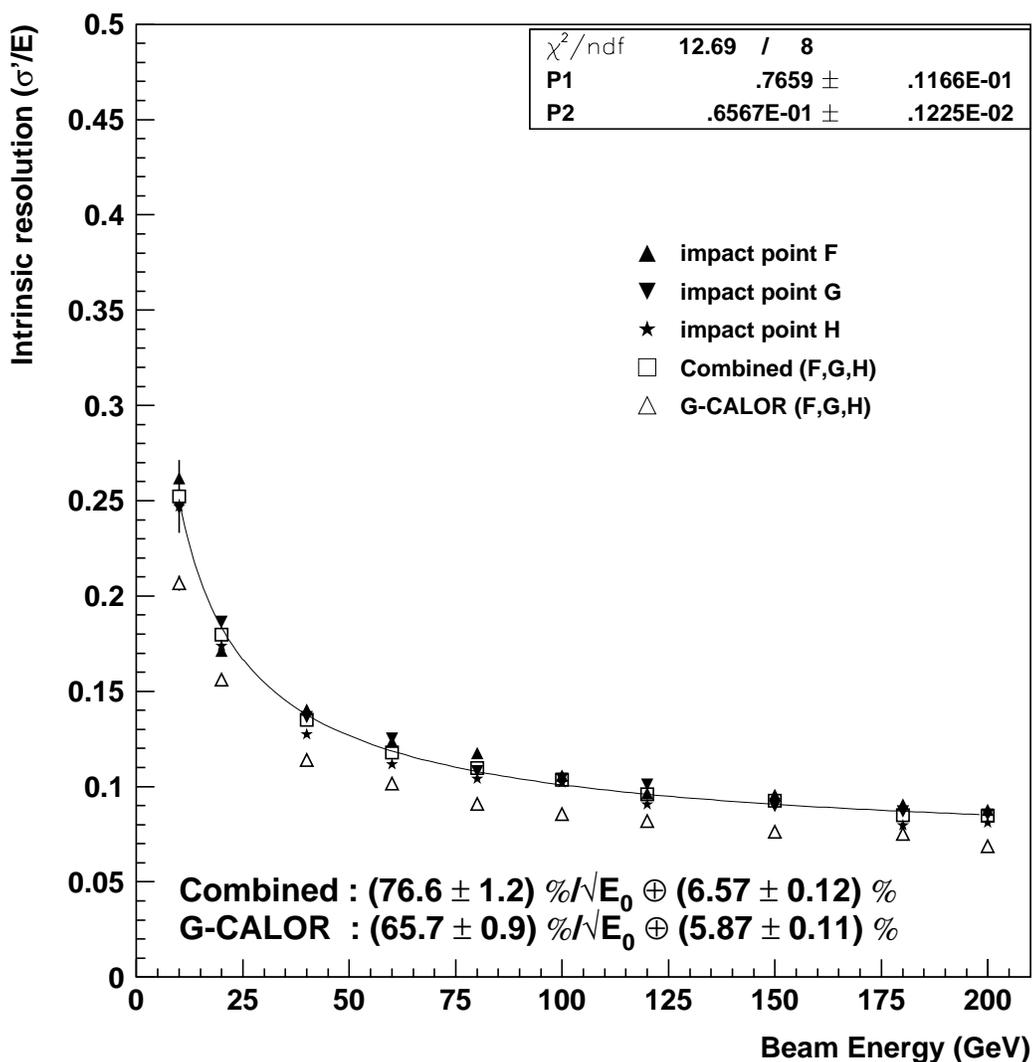
Figure 30: Combined pion intrinsic energy resolution vs. beam energy at impacts F, G and H. The error bars were calculated from the RMS deviation of the resolution at impact points F, G, and H. The resolution from Monte Carlo (G-CALOR) is also displayed. The line is the fit to the experimental data.
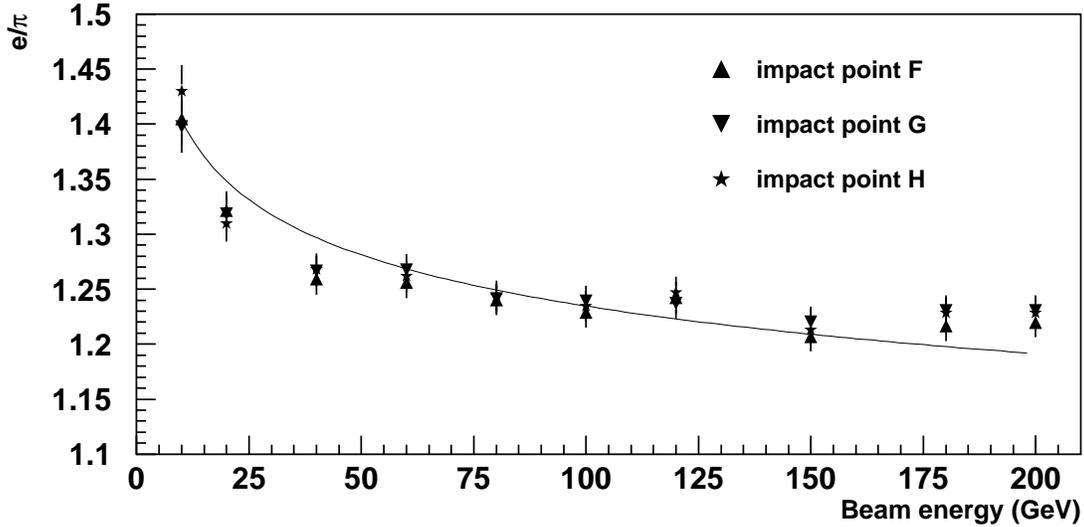
Figure 31: Energy dependence of the electron to pion response ratio *before* energy leakage corrections. The ratios for impact points F, G and H are presented. The line is the result of a fit to all the data points using Wigman's parameterization. The values of e/h obtained are presented in Table 6.

4.5 Determination of e/h

The ratio of electromagnetic to hadronic response, e/h, is a fundamental parameter which affects the calorimeter's intrinsic resolution to hadrons. The HEC is expected to be non-compensating ($e/h > 1$). This ratio cannot be measured directly, since the electromagnetic component f_{π^0} of hadronic shower varies as the logarithm of the energy. The ratio e/h can be estimated by studying the response of the calorimeter to pions, π. The latter is a combination of the purely electromagnetic (e) and hadronic (h) responses

$$\pi = e f_{\pi^0}(E) + h(1 - f_{\pi^0}(E)), \tag{11}$$

such that

$$\frac{e}{\pi} = \frac{e/h}{1 - (1 - \frac{e}{h})f_{\pi^0}(E)}, \tag{12}$$

where $f_{\pi^0}(E) = 0.11 \ln E(\text{GeV})$ [14]. The response to pions, $E_\pi(\text{nA})$, measured in Section 4.3 corresponds to π. Similarly, the response to electrons, $E_e(\text{nA})$, measured

in Section 3.3 corresponds to e. The ratio of the electron to pion response is then

$$\frac{e}{\pi} = \frac{\alpha_{em} E_e(\text{nA})}{\alpha_{em} E_\pi(\text{nA})} = \frac{E_0}{\alpha_{em} E_\pi(\text{nA})}. \tag{13}$$

After evaluating $f_{\pi^0}(E)$ at each energy and equating Equations 12 and 13, e/h is the only unknown parameter left. It can be extracted by a fit over the e/π data, as shown in Figure 31. Only the data for impacts points F, G and H are displayed. The analysis is not performed for impacts B and C because of their nearness with tie-rods which caused problems in evaluating α_{em} (see Section 3.3). Equation 12 used to estimate e/π, and hence e/h, assumes that the shower is fully contained within the detector. But Monte Carlo studies indicate that in the 1999 HEC beam test there is a leakage of the hadronic shower energy at the bottom of the calorimeter of about $(3.2 \pm 0.5)\%$ for any given beam energy (Section 4.3). This loss of energy produces an overestimate of the true e/h. The ratio of electromagnetic to hadronic response measured in Figure 31 can then be seen as the effective ratio of the responses, e/h_{eff}. The systematic error on α_{em}, mainly due to the observed small non-linearity of the electron response (see Section 3.3), dominates the final error on e/π. Since this error is highly correlated for all impact points at a given energy, a combined fit is performed on the average e/π calculated over impact points F, G, and H for each energy. The error on this average is taken from the average error on e/π for the 3 impact points. The results obtained for the 3 impact points studied and the combined fit are shown in Table 6.

The pion response is then corrected by including the leakage energy. The results obtained after correction are presented in Figure 32. The values of e/h extracted for the 3 impact points studied are shown in Table 6. The theoretical model is shown to agree better with the data after applying the correction as seen by the improved χ^2. The second error shown is due to the uncertainty on the energy leakage correction, and is estimated by varying the energy leakage by one standard deviation and re-performing the fits. The overall parameterization yields a ratio of $e/h = 1.509 \pm 0.021$, which is in agreement with the 2000 measurement [19] [16]. The

---

[19]A. Minaenko obtained an average measurement of $e/h = 1.50 \pm 0.05$ for the 2000 data.

Impact Position	e/h_{eff}	χ^2/ndf	e/h	χ^2/ndf
F	1.611 ± 0.014	$17.6/9$	$1.499 \pm 0.014 \pm 0.016$	$9.70/9$
G	1.626 ± 0.015	$23.8/9$	$1.513 \pm 0.014 \pm 0.016$	$11.0/9$
H	1.628 ± 0.014	$26.6/9$	$1.514 \pm 0.014 \pm 0.016$	$15.8/9$
Combined (F,G,H)	1.622 ± 0.014	$21.7/9$	$1.509 \pm 0.014 \pm 0.016$	$11.3/9$

Table 6: Electromagnetic to hadronic response ratio with energy leakage corrections (e/h) and without (e/h_{eff}). The correction for the energy leakage significantly improves the agreement with the parameterization. The systematic error on α_{em} dominates the final error on e/h_{eff}, whereas the error on e/h also depends significantly on the error on the energy leakage correction (second error).

e/h was also measured at each energy as shown in Figure 33.

Studies of the ATLAS calorimetry system have shown that measurements of e/h for fast readout calorimetry tends to be overestimated because of low energy cut-off and charge collection time [17]. Since the hadronic showers spread to several readout cells, the signal-to-noise ratio is poor in many of those readout cells creating a low energy cutoff, which leads to an overestimate of e/h. Also, the ATLAS hadronic calorimeters have been designed to operate with fast-readout of the signals, which causes the slow component of hadronic shower to be missed. Since there is no such slow process in electromagnetic showers, this again causes an overestimate of e/h. Although the value of e/h measured in this analysis pertains to the HEC as it will operate in ATLAS, care must be taken when comparing with other calorimeters.
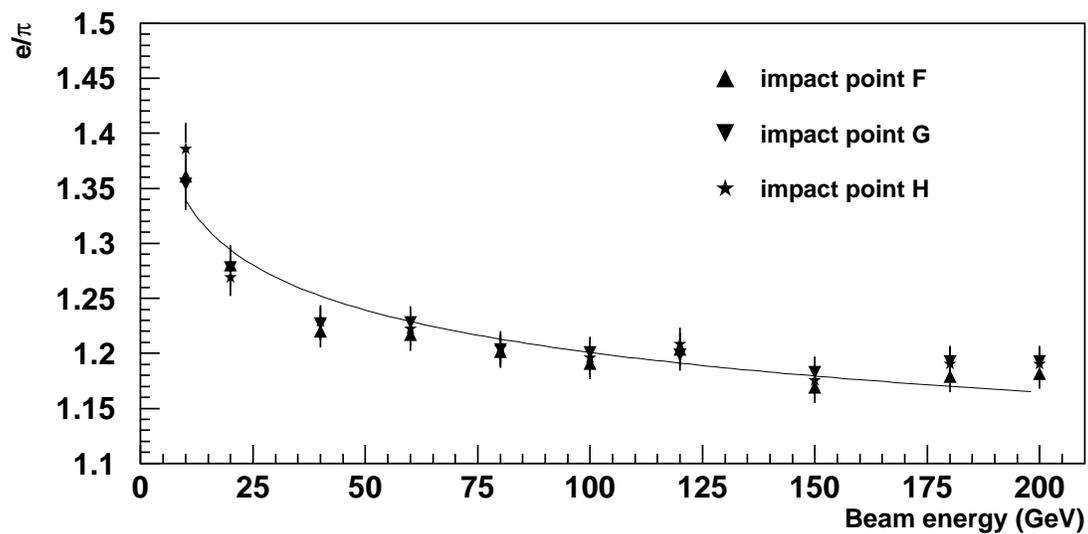
Figure 32: Energy dependence of the electron to pion response ratio *after* energy leakage corrections. The ratios for impact points F, G and H are presented. The line is the result of a fit to all the data points using Wigman's parameterization. The results obtained for e/h are presented in Table 6.
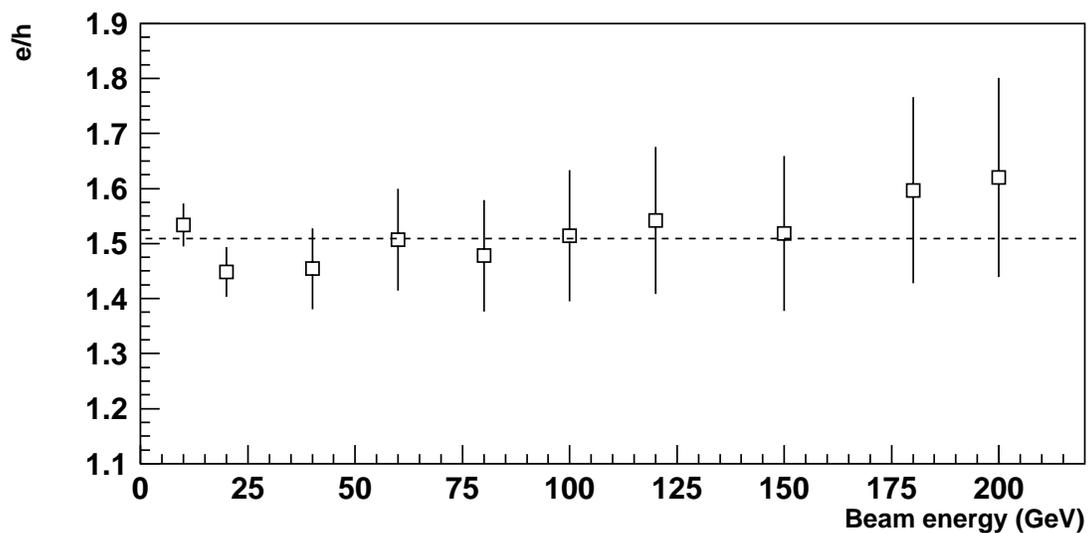

Figure 33: Individual measurement of e/h *after* energy leakage corrections for each of the 10 beam energies. The ratios obtained for impact point G only are presented. The dotted line represents the average e/h measured from a fit on all the data points using Wigman's parameterization.

5 Conclusions

During the summer of 1999, 6 complete modules (3 front and 3 rear wheel modules), or 3/32 of one of the two ATLAS Hadronic Endcap Calorimeters, were assembled and set in a beam test cryostat. This was the first time that production modules (modules which will be used in the construction of ATLAS) were tested and that the ATLAS cabling system was used. Some of these new electronic components, such as the Front End Boards, were not fully tested before the beam test and caused an increase of the electronic noise compare to previous years. The ATLAS calibration procedure was also followed for the first time.

The performance of the Hadronic Endcap Calorimeter is first evaluated using 10 to 193.1 GeV electron beams for five different impact positions. The response of the calorimeter is shown to be linear with energy within about one percent, and the electromagnetic constant is found to be $\alpha_{em} = (3.82 \pm 0.04)$ GeV/μA, which differs from previous measurements.

The intrinsic resolution (the resolution after electronic noise subtraction) of the calorimeter to electrons is then measured to be

$$\frac{\sigma'}{E} = \frac{(23.29 \pm 0.09)\%}{\sqrt{E_0(\text{GeV})}} \oplus (0.00 \pm 0.13)\%,$$

where E_0 is the initial particle energy, and E is the reconstructed energy. Furthermore, Monte Carlo simulations give an intrinsic resolution of

$$\frac{\sigma'}{E} = \frac{(20.7 \pm 0.4)\%}{\sqrt{E_0(\text{GeV})}} \oplus (0.67 \pm 0.11)\%.$$

Calibration problems are observed when the spatial uniformity of the calorimeter is studied. The response of two adjoining cells is studied and a 2.4% difference is observed. The response is also shown to be reduced for impacts closer to tie-rods, which explains the discrepancy in α_{em} and resolution measured for such impact positions.

The performance of the Hadronic Endcap Calorimeter is then evaluated using 10 to 200 GeV pion beams for five different impact positions. The response is

obtained using 54 cell clusters such that nearly full containment of hadronic showers is achieved. However, Monte Carlo simulations show that $(3.2 \pm 0.5)\%$ of the energy escapes, mainly at the bottom of the calorimeter. The intrinsic energy resolution (after electronic noise subtraction) of the calorimeter to pions is measured to be

$$\frac{\sigma'}{E} = \frac{(76.2 \pm 0.9)\%}{\sqrt{E_0(\text{GeV})}} \oplus (6.68 \pm 0.09)\%,$$

whereas Monte Carlo simulation yields an intrinsic resolution of

$$\frac{\sigma'}{E} = \frac{(64.5 \pm 0.8)\%}{\sqrt{E_0(\text{GeV})}} \oplus (5.51 \pm 0.1)\%.$$

Previous studies have shown that Monte Carlo simulations tend to predict a better resolution than that observed [15].

The differences observed between the results obtained in this analysis and previous measurements, or results from Monte Carlo simulations, are mainly due to the calibration procedure not being adequate in 1999 which caused the response to be different from one readout cell to another. The treatment of non-Gaussian tails in this analysis may have led to an underestimate of the effective electronic noise.

Finally, a study of the ratio of electromagnetic to hadronic response, e/h, is predicted. The hadronic response is corrected for leakage using Monte Carlo simulation results. This correction is found to improve the agreement between the theoretical model and the data, and yields

$$e/h = 1.509 \pm 0.021.$$

A   Layout Geometry of the HEC Readout Cells

The following figures display the geometric layout of the readout cells for the calorimeter [3]. Figure 34 show the distribution of the readout cells for the second depth (z=2) of the front wheel modules. The layout for the first depth (z=1) was presented in Figure 1. The distributions of the readout cells for the rear wheel modules (third and fourth depth) are shown in Figure 35.

24.06.99
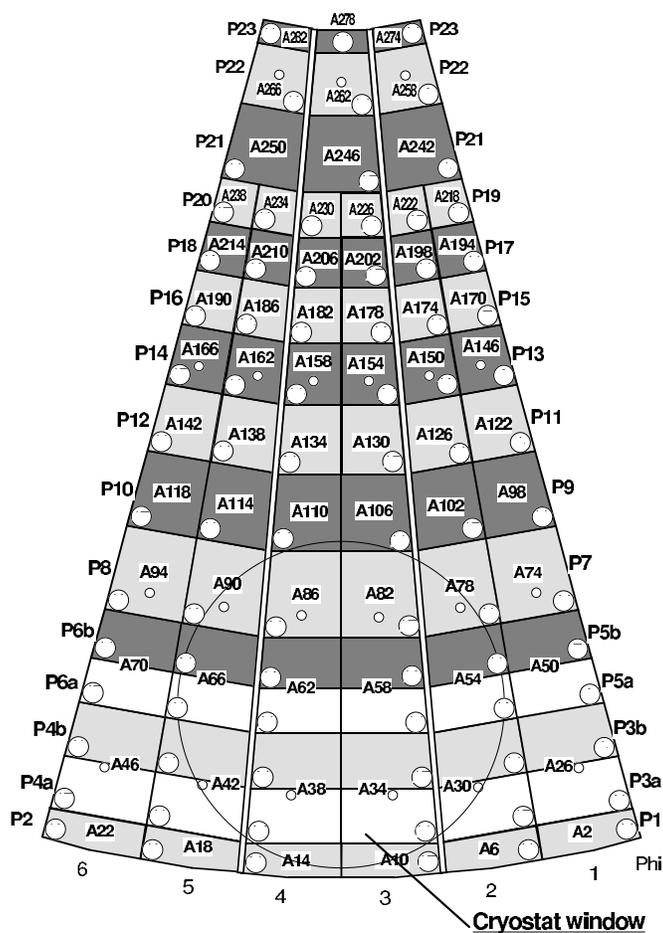
LSEG 2

Figure 34: The geometric layout of the readout cells for the second depth of the front wheel modules (z=2). The beam enters in a direction perpendicular to the surface shown, in a region behind the cryostat window. The numbers appearing in the squares and preceded by an "A" are identifying the channels used for the readout cells; the circled numbers are identifying the channels from the calibration generator.
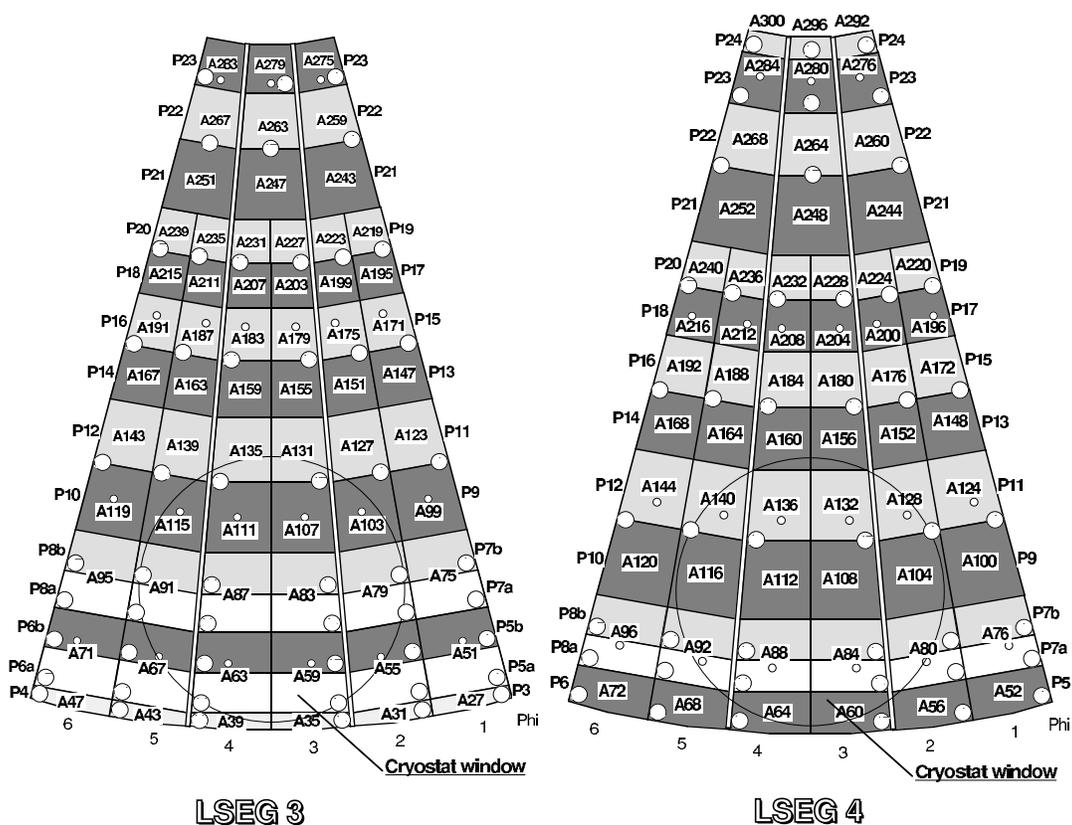
Figure 35: The geometric layout of the readout cells for the rear wheel modules (z=3 and z=4). The beam enters in a direction perpendicular to the surface shown, in a region behind the cryostat window. The numbers appearing in the squares and preceded by an "A" are identifying the channels used for the readout cells; the circled numbers are identifying the channels from the calibration generator.

B Error Analysis for the Intrinsic Energy Resolution

The formula for error expansion are summarized here. They were used in the calculation of the HEC intrinsic energy resolution, $r = \sigma'/E$, to electrons and pions (see Sections 3.5 and 4.4).

In order to extract the intrinsic resolution, the electronic cluster noise, σ_n, is subtracted out in quadrature from the width of the cluster response, σ,

$$\sigma' = \sigma \ominus \sigma_n = \sqrt{\sigma^2 - \sigma_n^2}, \tag{14}$$

such that the error on σ' is given by

$$(\Delta\sigma')^2 = \left(\frac{\sigma}{\sigma'}\right)^2 (\Delta\sigma)^2 + \left(\frac{\sigma_n}{\sigma'}\right)^2 (\Delta\sigma_n)^2. \tag{15}$$

The error on σ is purely statistical and originates from the Gaussian fit performed on the response, whereas the error on σ_n includes both the statistic and systematic error. Let μ_n be the cluster noise most probable current. The systematic errors on σ_n and μ_n are estimated as the difference between the best asymmetric fit obtained and the values obtained from a Gaussian fit performed in the region $\pm 2\sigma$ about the most probable current (see Section 2.3). The total error on σ_n and μ_n is the quadratic sum of this systematic and the statistical error.

Similarly, the HEC cluster response to electrons and pions was corrected for the cluster most probable current observed in the noise distribution (Sections 3.3 and 4.3). The corrected response, E, is

$$E = \mu_E - \mu_n, \tag{16}$$

where μ_E is the cluster response most probable current. The error on μ_n includes both the statistical and systematic error. Therefore, the error on E is given by

$$(\Delta E)^2 = (\Delta\mu_E)^2 + (\Delta\mu_n)^2. \tag{17}$$

Using all of the above results, the error on the intrinsic resolution is then given by

$$\left(\frac{\Delta r}{r}\right)^2 = \left(\frac{\Delta\sigma'}{\sigma'}\right)^2 + \left(\frac{\Delta E}{E}\right)^2. \tag{18}$$

References

[1] ATLAS Collaboration, "Liquid Argon Calorimeter Technical Design Report", *CERN/LHCC/96-41*, 15 December 1996.

[2] O'Neil, D., "Performance of the ATLAS Hadronic Endcap Calorimeter and The Physics of Electroweak Top Quark Production at ATLAS", Ph. D. Thesis, University of Victoria, 1999.

[3] Kindly provided by M. Kazarinov.

[4] Experimental Area Group, "Secondary Beamlines", information on the web at *http://sl.web.cern.ch/SL/eagroup/beams.html*

[5] M. Lefebvre, D. O'Neil and C. Sbarra, "The hec_adc package Version 3.8", update of *ATLAS HEC-Note-069*, p.18, November 2, 1999.

[6] Minaenko, A., "Analysis of August 99 TB data", Max-Plank-Institut für Physik, *HEC TB meeting*, December, 1999.

[7] Kurchaninov, L., "Electronics in TB-99, Max-Planck-Institut für Physik, *HEC/FCAL TB Analysis Meeting*, December, 1999.

[8] W.E. Cleland and E.G. Stern, "Signal processing considerations for liquid ionization calorimeters in a high rate environment", *Nucl. Inst. and Meth.*, **A338** (1994) 467-497.

[9] Particle Data Group, "Particle Physics Booklet", *European Physical Journal*, C3, 1998.

[10] A. Kiryunin and D. Salihgic, "Monte Carlo for the HEC Prototype: Software and Examples of Analysis", Max-Planck-Institut für Physik, *ATLAS HEC-Note-063*, November 25, 1998

[11] Kiryunin, A., "Test-Beam MC Simulation: Pions and Electrons", Max-Planck-Institut für Physik, *ATLAS HEC-Note-055*, September 24, 1998

[12] T.A. Gabriel and C. Zeitnitz, *Nucl. Inst. and Meth.*, **A349** (1987).

[13] M. Dobbs, M. Lefebvre and D. O'Neil, "Pion and Electron Energy Scan Analysis from April 1998 Testbeam Data", *ATL-LARG-99-001*, January 27, 1999.

[14] Wigmans, R., "On the energy resolution of uranium and other hadron calorimeters", *Nucl. Ins. Meth.*, **A259** (1987) 389-429.

[15] ATLAS Collaboration, "ATLAS detector and physics performance, Technical Design Report, Volume I", *CERN/LHCC/99-15*, Chapter 1, 25 May 1999.

[16] Minaenko, A., "HEC: Electron and Pion results from June 2000", Max-Plank-Institut für Physik, *HEC/FCAL TB Meeting*, September 20th, 2000.

[17] Juste, A., "Analysis of the Hadronic Performance of the TILECAL Prototype Calorimeter and Comparison with Monte Carlo", ATLAS Internal note, *TILECAL-95-069*, 1995.